A revised and expanded unified theory linking wall shear stress and vorticity topologies to enable the interpretation of cardiovascular flow disturbances

RESEARCH ARTICLE | MARCH 05 2025

A revised and expanded unified theory linking wall shear stress and vorticity topologies to enable the interpretation of cardiovascular flow disturbances

Valentina Mazzi ; Diego Gallo ; Karol Calò ; David A. Steinman ; Umberto Morbiducci

Physics of Fluids 37, 031907 (2025)
https://doi.org/10.1063/5.0253618

Physics of Fluids ARTICLE pubs.aip.org/aip/pof

A revised and expanded unified theory linking wall shear stress and vorticity topologies to enable the interpretation of cardiovascular flow disturbances

Cite as: Phys. Fluids **37**, 031907 (2025); doi: 10.1063/5.0253618
Submitted: 18 December 2024 · Accepted: 4 February 2025 ·
Published Online: 5 March 2025

Valentina Mazzi,[1] Diego Gallo,[1] Karol Calò,[1] David A. Steinman,[2] and Umberto Morbiducci[1,a)]

AFFILIATIONS

[1]PoliTo[BIO]Med Lab, Department of Mechanical and Aerospace Engineering, Politecnico di Torino, Turin, Italy
[2]Biomedical Simulation Laboratory, Department of Mechanical & Industrial Engineering, University of Toronto, Toronto, Ontario, Canada

[a)]Author to whom correspondence should be addressed: umberto.morbiducci@polito.it

ABSTRACT

Deciphering the complex interactions at the blood vessel–wall interface remains a key challenge in hemodynamics research. Wall shear stress (WSS) is recognized as a signature for near-wall velocity dynamics, while vorticity represents a fundamental structure of fluid motion. In this work, we revise and extend a recently proposed unifying theoretical approach that sought to connect the topological features of surface vorticity (SV) and WSS [Mazzi, Gallo, Calò, Steinman, and Morbiducci, "Linking wall shear stress and vorticity topologies: Toward a unified theory of cardiovascular flow disturbances," Phys. Fluids **36**(6), 61905 (2024)], the latter recently gaining momentum as a predictor of vascular disease. By revising a partially erroneous interpretation of the link between WSS and SV fixed points (focal points on the luminal surface where these fields vanish), we demonstrate here that every WSS fixed point is also a SV fixed point, and vice versa, though their nature and stability may differ. Building upon the previous study, we establish a robust theoretical classification of the possible combinations of WSS and SV fixed points, based on their nature and stability, and mechanistically connect them to near-wall fluid structures. These structures can further be distinguished by the presence or absence of vorticity diffusion flux normal to the wall, depending on local vorticity kinematics. High-resolution computational fluid dynamics simulations on intracranial aneurysm models validate these theoretical insights. This unifying framework offers a clear taxonomy describing the mechanistic relationship between near-wall flow disturbances and intravascular hemodynamics, providing a deeper understanding of how local shear forces are influenced by near-wall fluid structures, while also paving the way for a clearer interpretation of the role of near-wall hemodynamics in vascular pathophysiology.

I. INTRODUCTION

A complicated interplay of systemic, biological, and hemodynamic factors underpins the onset and progression of a plethora of vascular diseases.[1] In the intricate landscape of vascular pathophysiology, local hemodynamics has long been recognized as playing a pivotal role[2–8] due to the mechanisms of action of flow disturbances on the endothelium. Attention has been directed toward the hemodynamics in the near-wall region, which is involved in regulating the local transport of biochemicals at the interface between the streaming blood and the arterial wall,[4] as well as in the mechanical stimulation of the endothelium. This is traditionally interpreted in terms of wall shear stress,[9] which modulates endothelial function through the activation of the mechanotransduction machinery regulating endothelial cells gene expression and response via specialized signaling pathways.[10]

In efforts to unveil the mechanisms underlying vascular pathophysiology involving local hemodynamics, the multifaceted nature of the wall shear stress has been extensively investigated over the years and several quantities traceable to wall shear stress have been proposed as localizing factors influencing vascular wall dysfunction, as well as potential markers/predictors of vascular disease. However, despite the large body of literature on the topic, a still unclear picture emerges, characterized by only moderate and sometimes contradictory associations between vascular disease and wall shear stress.[11–13] In recent years, there has been growing research interest in analyzing the topological skeleton wall shear stress applied to cardiovascular flows.[9,14–20] Peculiar wall shear stress topological features have emerged as predictors of future myocardial infarction,[6] long-term restenosis risk following carotid surgical interventions,[21] and early-stage plaque progression

in coronary arteries.[8,22] Additionally, the analysis of the wall shear stress topological skeleton has provided insights into blood–wall mass transfer in vascular territories.[9,23,24]

Applying dynamical systems theory to the shear forces at the fluid–wall interface, the wall shear stress topological skeleton is composed of fixed (or critical) points where wall shear stress locally vanishes and around which the wall shear stress field lines can adopt a finite number of distinct configurations. Additionally, there are unstable and stable manifolds (or critical lines) that link these fixed points, along which the wall shear stress field lines thicken or rarefy, exerting a contraction or expansion action on the endothelium.[15] Interpreting the topological skeleton of wall shear stress in terms of biomechanical actions on the endothelium is biologically relevant because the wall shear stress topology reflects key hemodynamic features such as flow separation, stagnation, and impingement points, which have been identified as biomechanical factors contributing to vascular disease.[14,15]

A. Linking wall shear stress profiles to intravascular fluid structures

While there is active research exploring the association between vascular adverse events and the frictional forces exerted by the flowing blood at the blood–wall interface, relatively few studies have focused on clearly identifying the intravascular fluid structures that, by leaving their distinctive imprints on the vessel wall, decisively shape the topological skeleton of wall shear stress. In this context, fluid mechanics theory points to vorticity[25] to uncover the intravascular fluid structures that shape wall shear stress topology. Specifically, the physiological significance of vorticity transport and vorticity-derived quantities, such as helicity, has been interpreted in terms of energetics, demonstrating beneficial effects, for instance, in the hemodynamics of the heart[26,27] and the aorta,[28,29] as well as in terms of atheroprotective action on the endothelium,[30–32] contributing to maintaining physiologic transport of biochemicals and mechanical stress distribution.[33] Alongside this beneficial impact, certain vorticity-related quantities have also been implicated in detrimental effects, such as in coronary arteries,[34–36] and in intracranial[17,37–41] and abdominal aortic aneurysms.[42–44]

Motivated by the need to understand how intravascular fluid structures shape wall shear stress on the luminal surface of the vessel, we recently proposed a unified theory to link vorticity to wall shear stress profiles.[45] The study's rationale was that elucidating the connections between the topological skeletons of wall shear stress and surface vorticity (the vorticity on the luminal surface of the vessel) could provide a key for deciphering the nature of the local interactions between intravascular hemodynamics and the vessel wall. This, in turn, would offer a clear interpretation of the phenomena occurring at the lumen–endothelium interface and would contribute to a less elusive definition of the "flow disturbances" implicated in adverse biological events.[45] To achieve this, we drew inspiration from existing theories on the structure of turbulence in the boundary layer at no-slip walls[46,47] and sought to establish a definitive theoretical link between the topological features of wall shear stress and surface vorticity, differentiating cases based on at-wall and near-wall vorticity characteristics.[45] Among the main findings of that study, we demonstrated that (i) the location, nature, and stability of wall shear stress and surface vorticity fixed points are tightly connected, and (ii) the near-wall vorticity characteristics are closely tied to the theoretically possible specific permutations of wall shear stress and surface vorticity fixed points.[45] Unfortunately, we also mistakenly considered a scenario where the normal component of the surface vorticity could take on a not-null value, leading us to the erroneous conclusion, that in some cases, wall shear stress fixed points might not have corresponding surface vorticity fixed points.[45]

B. Revising and expanding the link between wall shear stress and surface vorticity

In this study, all wall shear stress and surface vorticity fixed points configurations as outlined in our previous study[45] are revisited, correcting an erroneous interpretation regarding a property characterizing vorticity. Furthermore, we expand upon the previous theory[45] by introducing new types of wall shear stress and surface vorticity fixed points, along with their connections with near-wall fluid structures. To demonstrate the impact of the revised theory when applied to cardiovascular flows, we use the same high-fidelity computational fluid dynamics (CFD) simulations of intracranial aneurysm hemodynamics as in our previous study.[45] The revised and expanded theory presented here offers a comprehensive taxonomy of the near-wall velocity and vorticity kinematics shaping the shear stress topology onto the luminal surface of a vessel.

II. METHODS

A. Theoretical remarks

This section provides the theoretical background for a better understanding of the theory adopted in this study to properly revise and extend the theory underpinning the relationship between the topology of the wall shear stress and surface vorticity in cardiovascular flows demonstrated in the previous study.[45]

1. Wall shear stress vs surface vorticity

Let $\Omega \subset \mathbb{R}^3$ be a domain representing the lumen of a vessel. For a Newtonian fluid, the wall shear stress $\boldsymbol{\tau}$ on the surface boundary $\partial\Omega$ (from this point onward, $\partial\Omega$ will refer solely to the vessel wall, excluding the inflow and outflow sections) can be defined as:

$$\boldsymbol{\tau} = \mathbb{P} \cdot (-2\,\mu\,\boldsymbol{n} \cdot \boldsymbol{S}_{\partial\Omega}), \tag{1}$$

where μ is the dynamic viscosity, $\boldsymbol{n}$ is the unit vector normal to the surface boundary $\partial\Omega$ directed from the wall toward the fluid, and $\boldsymbol{S}_{\partial\Omega}$ is the strain rate tensor on $\partial\Omega$, which can be expressed in terms of the fluid velocity vector $\boldsymbol{u}$ as follows:

$$\boldsymbol{S}_{\partial\Omega} = \frac{1}{2}\left(\nabla \boldsymbol{u}_{\partial\Omega} + \nabla \boldsymbol{u}_{\partial\Omega}^{T}\right). \tag{2}$$

In eq. (1) $\mathbb{P}$ is the tangential projection operator:

$$\mathbb{P} = I - \boldsymbol{n} \otimes \boldsymbol{n}, \tag{3}$$

where I is the identity matrix.

As the velocity gradient tensor $\nabla \boldsymbol{u}_{\partial\Omega}$ can be decomposed into the sum of its symmetric [$\boldsymbol{S}_{\partial\Omega}$, in Eq. (2)] and skew-symmetric ($\boldsymbol{W}_{\partial\Omega} = \frac{1}{2}(\nabla \boldsymbol{u}_{\partial\Omega} - \nabla \boldsymbol{u}_{\partial\Omega}{}^{T})$) parts:

$$\begin{aligned}\nabla \boldsymbol{u}_{\partial\boldsymbol{\Omega}} &= \boldsymbol{S}_{\partial\boldsymbol{\Omega}} + \boldsymbol{W}_{\partial\boldsymbol{\Omega}} \\ &= \frac{1}{2}\left(\nabla \boldsymbol{u}_{\partial\boldsymbol{\Omega}} + \nabla \boldsymbol{u}_{\partial\boldsymbol{\Omega}}{}^{T}\right) + \frac{1}{2}\left(\nabla \boldsymbol{u}_{\partial\boldsymbol{\Omega}} - \nabla \boldsymbol{u}_{\partial\boldsymbol{\Omega}}{}^{T}\right),\end{aligned} \tag{4}$$

it follows that $\nabla \boldsymbol{u}_{\partial\Omega}^T = \boldsymbol{S}_{\partial\Omega} - \boldsymbol{W}_{\partial\Omega}$, and that the strain rate tensor $\boldsymbol{S}_{\partial\Omega}$ can then be expressed in terms of $\boldsymbol{W}_{\partial\Omega}$, i.e.:

$$\boldsymbol{S}_{\partial\boldsymbol{\Omega}} = \nabla \boldsymbol{u}_{\partial\boldsymbol{\Omega}}^T + \boldsymbol{W}_{\partial\boldsymbol{\Omega}}. \tag{5}$$

By substituting Eq. (5) in Eq. (1), the expression for $\boldsymbol{\tau}$ can be reformulated as follows:

$$\begin{aligned}\boldsymbol{\tau} &= \mathbb{P} \cdot \left[-2\,\mu\,\boldsymbol{n} \cdot \left(\nabla \boldsymbol{u}_{\partial\boldsymbol{\Omega}}^T + \boldsymbol{W}_{\partial\boldsymbol{\Omega}}\right)\right] \\ &= \mathbb{P} \cdot \left[2\,\mu\left(-\boldsymbol{n} \cdot \nabla \boldsymbol{u}_{\partial\boldsymbol{\Omega}}^T - \boldsymbol{n} \cdot \boldsymbol{W}_{\partial\boldsymbol{\Omega}}\right)\right].\end{aligned} \tag{6a}$$

According to the definition of the surface deformation stress $\boldsymbol{t}_s$,[48] and considering blood as incompressible, it follows that on the rigid surface $\partial\Omega$, $\boldsymbol{t}_s = -2\mu\boldsymbol{n} \cdot (\nabla \cdot \boldsymbol{u}_{\partial\Omega}\,\mathbf{I} - \nabla \boldsymbol{u}_{\partial\Omega}^T)$, where $\mathbf{I}$ is the unit tensor, results in a null vector. Consequently, the term $2\,\mu\,\boldsymbol{n} \cdot \nabla \boldsymbol{u}_{\partial\Omega}^T$ in Eq. (6a) is null. Furthermore, by exploiting the skew-symmetric property of the spin tensor, ($\boldsymbol{W}_{\partial\Omega} = -\boldsymbol{W}_{\partial\Omega}^T$), Eq. (6a) can be reformulated as follows:

$$\begin{aligned}\boldsymbol{\tau} &= \mathbb{P} \cdot \left[2\,\mu\,(-\boldsymbol{n} \cdot \boldsymbol{W}_{\partial\boldsymbol{\Omega}})\right] = \mathbb{P} \cdot \left[2\,\mu\left(\boldsymbol{n} \cdot \boldsymbol{W}_{\partial\boldsymbol{\Omega}}^T\right)\right] \\ &= \mathbb{P} \cdot \left[2\,\mu\,(\boldsymbol{W}_{\partial\boldsymbol{\Omega}} \cdot \boldsymbol{n})\right].\end{aligned} \tag{6b}$$

For any generic vector $\boldsymbol{\xi}$, the spin tensor $\boldsymbol{W}_{\partial\Omega}$ satisfies the well-known relation:

$$2\boldsymbol{W}_{\partial\Omega} \cdot \boldsymbol{\xi} = \boldsymbol{\omega}_{\partial\Omega} \times \boldsymbol{\xi}, \tag{7}$$

where $\boldsymbol{\omega}_{\partial\Omega}$ is the surface vorticity, i.e., the vorticity on the luminal surface of the vessel. The veracity of Eq. (7) has already been proven elsewhere.[45]

From Eq. (7), it follows that Eq. (6b) can be reformulated as:

$$\boldsymbol{\tau} = \mathbb{P} \cdot (\,\mu\,\boldsymbol{\omega}_{\partial\boldsymbol{\Omega}} \times \boldsymbol{n}). \tag{8}$$

Finally, based on the definition of $\mathbb{P}$ from Eq. (3), Eq. (8) can be reformulated as follows:

$$\begin{aligned}\boldsymbol{\tau} &= (I - \boldsymbol{n} \otimes \boldsymbol{n}) \cdot (\,\mu\,\boldsymbol{\omega}_{\partial\boldsymbol{\Omega}} \times \boldsymbol{n}\,) \\ &= (\mu\,\boldsymbol{\omega}_{\partial\Omega} \times \boldsymbol{n}) - (\boldsymbol{n} \otimes \boldsymbol{n}) \cdot (\,\mu\,\boldsymbol{\omega}_{\partial\Omega} \times \boldsymbol{n}\,) \\ &= (\mu\,\boldsymbol{\omega}_{\partial\Omega} \times \boldsymbol{n}) - [(\mu\,\boldsymbol{\omega}_{\partial\Omega} \times \boldsymbol{n}) \cdot \boldsymbol{n}] \\ &= \mu\,\boldsymbol{\omega}_{\partial\Omega} \times \boldsymbol{n},\end{aligned} \tag{9}$$

where the term $(\mu\,\boldsymbol{\omega}_{\partial\Omega} \times \boldsymbol{n}) \cdot \boldsymbol{n}$ is trivially equal to zero, since the vectors $(\mu\,\boldsymbol{\omega}_{\partial\Omega} \times \boldsymbol{n})$ and $\boldsymbol{n}$ are orthogonal by construction.

A consequence of Eq. (9) is that the pair ($\boldsymbol{\tau}$, $\boldsymbol{\omega}_{\partial\Omega}$) is orthogonal on the luminal surface $\partial\Omega$ [Fig. 1(A)]. Moreover, based on Eq. (9), the wall shear stress $\boldsymbol{\tau}$ can be interpreted not only in terms of near-wall velocity dynamics,[49] but also in terms of vorticity $\boldsymbol{\omega}$.[45]

Fluid vorticity $\boldsymbol{\omega}$ in domain Ω is a solenoidal vector field, i.e., it satisfies the equation:

$$\nabla \cdot \boldsymbol{\omega} = 0 \tag{10}$$

everywhere in Ω. Moreover, contrary to what we reported in Ref. 45, the surface vorticity $\boldsymbol{\omega}_{\partial\Omega}$ satisfies the following condition:

$$\boldsymbol{\omega}_{\partial\Omega} \cdot \boldsymbol{n} = 0 \tag{11}$$

everywhere on $\partial\Omega$,[50] because the fluid velocity obeys the no-slip condition. Hence, Eq. (11) implies that the surface vorticity $\boldsymbol{\omega}_{\partial\Omega}$ always has a null component normal to $\partial\Omega$.

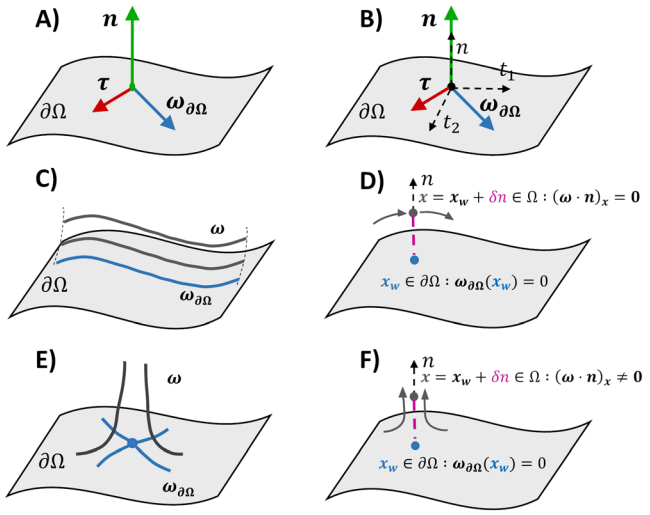

FIG. 1. (A) Sketch of wall shear stress (red arrow) and surface vorticity (blue arrow) vectors forming an orthogonal pair ($\boldsymbol{\tau}$, $\boldsymbol{\omega}_{\partial\Omega}$) on a stationary curved wall $\partial\Omega$; (B) local coordinate system (t_1, t_2, n) such that the $t_1 - t_2$ plane identifies the local tangent plane to $\partial\Omega$; (C) vortex lines infinitesimally close to a wall aligned parallel to the wall; (D) sketch of the presence of a null vorticity flux normal to the wall; (E) turning of tangential vortex lines to the normal direction; (F) sketch of the presence of a not-null vorticity flux normal to the wall. The blue vortex lines represent surface vorticity.

The properties expressed by Eqs. (10) and (11) are not violated if, when expressing the vorticity vector $\boldsymbol{\omega}$ near the wall in the local coordinate system (t_1, t_2, n), where n is normal to $\partial\Omega$ and t_1 and t_2 are orthogonal directions on $\partial\Omega$ [Fig. 1(B)], the vorticity gradient in the direction normal to $\partial\Omega$, which can be formulated as $\frac{\partial}{\partial n}(\boldsymbol{\omega} \cdot \boldsymbol{n})$, assumes a not null value.

The consequence of satisfying the condition $\frac{\partial}{\partial n}(\boldsymbol{\omega} \cdot \boldsymbol{n}) \neq 0$ is that, in the near-wall region, a vorticity diffusion flux normal to the luminal surface $\partial\Omega$ is established. Based on Eqs. (10) and (11), the vorticity diffusion flux σ_n can be expressed as:

$$\begin{aligned}\sigma_n &= \nu\,\frac{\partial}{\partial n}(\boldsymbol{\omega} \cdot \boldsymbol{n}) = -\nu\,\nabla_\pi \cdot \boldsymbol{\omega} \\ &= -\nu\left[\frac{\partial}{\partial t_1}(\boldsymbol{\omega} \cdot \boldsymbol{t}_1) + \frac{\partial}{\partial t_2}(\boldsymbol{\omega} \cdot \boldsymbol{t}_2)\right],\end{aligned} \tag{12}$$

where ν is the kinematic viscosity and ∇_π represents the surface gradient along the tangential direction to the surface. The vorticity diffusion flux, deriving from the viscous term in the vorticity transport equation,[51] measures the amount of vorticity diffused in or out $\partial\Omega$ per unit area and unit time and describes the kinematic evolution of the vorticity. Equation (12), where all quantities on the right side are defined on $\partial\Omega$, expresses the normal derivatives in terms of the tangent ones.

The physical interpretation of Eq. (12) is that σ_n represents a purely kinematic effect of Eq. (10).[50] Upon closer inspection, it can be argued that there are only two possible ways of interaction of the vorticity with a material surface: (i) vortex lines in the near-wall region are aligned parallel to the wall [Fig. 1(C)], and the vorticity diffusion flux σ_n normal to the luminal surface $\partial\Omega$[50] must be null [case $\sigma_n = 0$, Fig. 1(D)]; (ii) the near-wall vortex lines deflect from parallel to normal

to the wall, or vice versa [Fig. 1(E)], thereby establishing a not-null vorticity diffusion flux normal to the material surface [case $\sigma_n \neq 0$, Fig. 1(F)]. Interestingly, when $\sigma_n \neq 0$, the existence of a vorticity flux normal to the wall in the near-wall region can be associated with a not-null curl of the wall shear stress on the material surface, as supported by the following expression (the proof of which is presented in the Appendix):

$$\boldsymbol{\sigma_n} = -\nu \nabla_{\boldsymbol{\pi}} \cdot \boldsymbol{\omega} = \frac{\boldsymbol{n}}{\rho} \cdot (\nabla \times \boldsymbol{\tau}), \tag{13}$$

where ρ is the density. A physical interpretation of Eq. (13) is that the tendency to rotation of the wall shear stress $\boldsymbol{\tau}$ on the material surface $\partial\Omega$ always results in a deflection of vortex lines from being parallel to normal to the wall (or vice versa, depending on the direction of rotation of $\boldsymbol{\tau}$) in the near-wall region.

2. The topological skeleton of a vector field

Equation (9) implies a strong relationship between the topological skeletons of $\boldsymbol{\tau}$ and $\boldsymbol{\omega}_{\partial\Omega}$. Recently, we proposed that a clear interpretation of this relationship could provide insights into how blood flow dynamics shape the wall shear stress topology on the vessel wall,[6,21,22] which has been identified as a contributing factor in the onset and progression of vascular disease.[6,21,22] Rooted in dynamical system theory, a topological skeleton of a vector field consists of a collection of fixed points $\boldsymbol{x}_{fp} \in \mathbb{R}^n$(critical points where the field locally vanishes) connected by stable/unstable manifolds (or critical lines) that repel/attract nearby field lines [Fig. 2(A)].

Fixed points play a pivotal role in shaping the structure of the topological skeleton, as a result of their stability properties [Fig. 2(B)]: a stable/unstable fixed point is characterized by a sink/source configuration, attracting/repelling the nearby field lines.[14–16] Beyond stability, fixed points can be further classified into saddle points, foci, centers, or nodes [Fig. 2(B)]: (i) a saddle point attracts and repels nearby field lines along two distinct directions; (ii) a stable/unstable focus is encased within converging/diverging and spiral-shaped field lines; (iii) a center is enclosed by field lines forming closed loops; (iv) a stable/unstable node exhibits converging/diverging field lines [Fig. 2(B)]. For fixed points classified as nodes, two special cases exist: the stable/unstable star node, characterized by converging/diverging straight field lines, and the stable/unstable degenerate node, which attracts/repels field lines collapsing along a primary direction [Fig. 2(B)].[52]

TABLE I. Classification of fixed points based on the eigenvalues of the Jacobian matrix for a 2D vector field ($\alpha, \beta \in \mathbb{R}^+$). I is the identity matrix.

Λ	Fixed point
$\lambda_1 < 0 < \lambda_2$	Saddle point
$\lambda_1, \lambda_2 > 0$	Unstable node
$\lambda_1, \lambda_2 < 0$	Stable node
$\lambda_1 = \lambda_2 > 0,\ J = \lambda I$	Unstable star node
$\lambda_1 = \lambda_2 < 0,\ J = \lambda I$	Stable star node
$\lambda_1 = \lambda_2 > 0,\ J \neq \lambda I$	Unstable degenerate node
$\lambda_1 = \lambda_2 < 0,\ J \neq \lambda I$	Stable degenerate node
$\lambda_{1,2} = \alpha \pm \beta \mathrm{i}$	Unstable focus
$\lambda_{1,2} = -\alpha \pm \beta \mathrm{i}$	Stable focus
$\lambda_{1,2} = \pm \beta \mathrm{i}$	Center

Starting from the observation that the orthogonal pair $(\boldsymbol{\tau}, \boldsymbol{\omega}_{\partial\Omega})$ lies on $\partial\Omega$, a two-dimensional analysis can be employed to identify and classify fixed points, determining their nature and stability properties. Technically, fixed points can be identified by computing the Poincaré index,[53] as extensively detailed in previous studies.[15,16,45] While the Poincaré index locates fixed points, it does not provide information about their nature or stability properties.

The classification of fixed points requires analyzing the signs of the eigenvalues λ_i of the Jacobian matrix J of the vector field.[16,54] This process, summarized in Table I, considers the $\boldsymbol{\tau}$ and $\boldsymbol{\omega}_{\partial\Omega}$ fields within the two-dimensional space of the luminal surface (Fig. 1).

As reported in Table I, star and degenerate nodes are special cases of nodes where the eigenvalues of the Jacobian matrix are real and

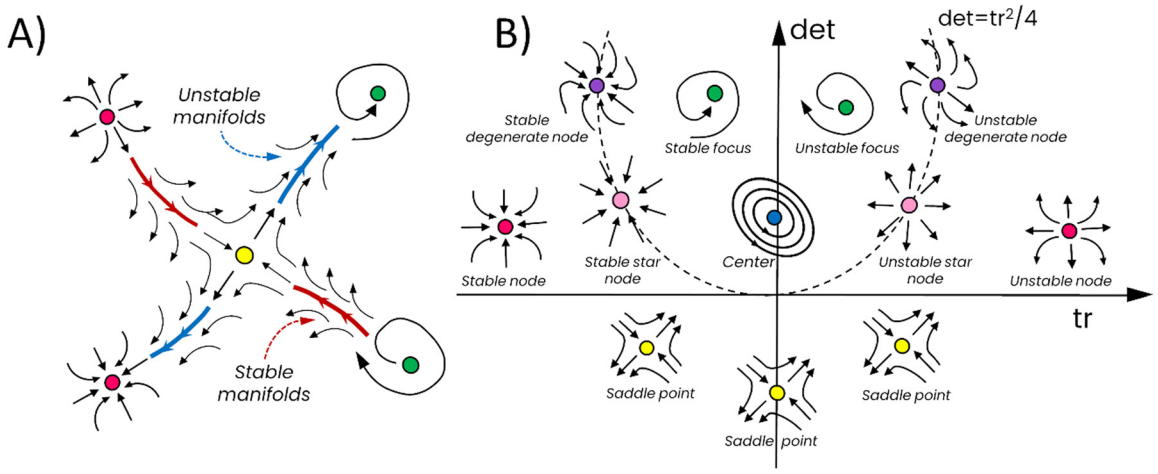

FIG. 2. (A) Explanatory sketch of the stable/unstable manifold configurations linking fixed points; (B) stability and type of fixed points of a vector field in the tr-det plane, where tr and det refer to the trace and determinant of the Jacobian matrix of the vector field respectively. The dotted line represents the *critical quadratic curve* splitting the det > 0 region in two subregions where the eigenvalues of the Jacobian matrix of the vector field are complex or real numbers. Inspired by Perry and Fairlie.[64]

coincide. Additionally, the Jacobian matrix is either proportional or non-proportional to the identity matrix for star and degenerate nodes, respectively.

In general, the eigenvalues λ_i of the Jacobian matrix J are the roots of the characteristic polynomial $p_J(\lambda) = \det(J - \lambda I)$. In the case of interest, for a 2×2 Jacobian matrix, the characteristic polynomial can be expressed in terms of the trace and determinant as follows:

$$\lambda^2 - \mathrm{tr}(J)\lambda + \det(J) = 0, \tag{14}$$

where $\mathrm{tr}(J) = \lambda_1 + \lambda_2$ and $\det(J) = \lambda_1\lambda_2$. To summarize the theoretical remarks presented in Table I and Fig. 2(B), the analysis of the Jacobian matrix of the field reveals that if $\det(J) < 0$, the fixed point is a saddle point. In the case $\det(J) > 0$, the fixed point can be a focus, a node, or a center, specifically: (i) if $\det(J) > \frac{\mathrm{tr}^2(J)}{4}$, the fixed point is a focus; (ii) if $\det(J) < \frac{\mathrm{tr}^2(J)}{4}$, the fixed point is a node; (iii) if $\det(J) = \frac{\mathrm{tr}^2(J)}{4}$, the fixed point is star or a degenerate node; (iv) if $\mathrm{tr}(J) = 0$, the fixed point is a center.

Finally, in the case of a node or a focus, the stability of the fixed point is determined by the sign of $\mathrm{tr}(J)$, with $\mathrm{tr}(J) < 0$ identifying a stable fixed point and $\mathrm{tr}(J) > 0$ identifying an unstable one.

B. Wall shear stress and surface vorticity fixed points

In this section, we analyze the relationship between the location, nature and stability properties of fixed points of the orthogonal pair $(\boldsymbol{\tau}, \boldsymbol{\omega}_{\partial\Omega})$, partially revising and extending the conclusions from a recent study from the authors.[45] According to Eqs. (9) and (11), in the local coordinate system (t_1, t_2, n) illustrated in Fig. 1(B), the wall shear stress $\boldsymbol{\tau}$ can be expressed in terms of the surface vorticity components $\boldsymbol{\omega}_{\partial\Omega} = (\omega_{t_1}, \omega_{t_2}, 0)$ as follows:

$$\begin{aligned}\boldsymbol{\tau} = (\tau_{t_1}, \tau_{t_2}, 0) = \mu\boldsymbol{\omega}_{\partial\Omega} \times \boldsymbol{n} = \mu\det\begin{pmatrix} t_1 & t_2 & n \\ \omega_{t_1} & \omega_{t_2} & 0 \\ 0 & 0 & 1 \end{pmatrix} \\ = (\boldsymbol{\mu\omega}_{t_2}, -\boldsymbol{\mu\omega}_{t_1}, 0).\end{aligned} \tag{15}$$

From Eq. (15), it follows that:

$$\forall \tilde{\boldsymbol{x}} \in \partial\Omega : \boldsymbol{\tau}(\tilde{\boldsymbol{x}}) = 0 \iff \boldsymbol{\omega}_{\partial\Omega}(\tilde{\boldsymbol{x}}) = 0. \tag{16}$$

Contrary to our earlier study,[45] where we mistakenly stated that in some cases the fixed points of $\boldsymbol{\tau}$ might not correspond to fixed points of $\boldsymbol{\omega}_{\partial\Omega}$, the key implication of Eq. (16) is that if $\tilde{\boldsymbol{x}} \in \partial\Omega$ is a fixed point for $\boldsymbol{\tau}$, $\tilde{\boldsymbol{x}}$ must also be a fixed point for $\boldsymbol{\omega}_{\partial\Omega}$, and vice versa. However, this bijective relationship in Eq. (16) does not necessarily imply that fixed points for $\boldsymbol{\tau}$ and $\boldsymbol{\omega}_{\partial\Omega}$ at $\tilde{\boldsymbol{x}}$ will share the same nature and stability properties. Therefore, a deeper investigation is required to elucidate the relationship between the fixed points of $\boldsymbol{\tau}$ and $\boldsymbol{\omega}_{\partial\Omega}$ at $\tilde{\boldsymbol{x}}$, as the nature and stability of fixed points are critical in shaping the topological skeleton of both fields on the luminal surface, which reflect the near-wall velocity and vorticity dynamics. In detail, as the topological skeleton of wall shear stress provides a signature for the near-wall velocity,[49] a sink (source) configuration for $\boldsymbol{\tau}$ around one of its fixed points indicates the presence of a fluid structure in the near-wall that tends to move away from (toward) the wall. Similarly, when the topological skeleton of $\boldsymbol{\omega}_{\partial\Omega}$ is characterized by a sink (source) configuration around one of its fixed points, the near-wall vorticity is expected to feature vortex lines that move away from (toward) the wall. From this point forward, as in our previous study,[45] we will use the expressions "emanating from" and "impinging on" to refer to field lines that move away from and toward the wall, respectively. Based on these insights, it becomes clear that analyzing a fixed point on $\partial\Omega$ provides a crucial key for interpreting the near-wall velocity and vorticity dynamics, and ultimately the types of fluid structures interacting with the vessel wall.[16,54]

The subsections below deal with the analysis of wall shear stress and surface vorticity fixed points in cases where σ_n, the vorticity diffusion flux normal to the wall [Eq. (12)], is either null [Fig. 1(C)], or not null [Fig. 1(E)].

1. Wall shear stress and surface vorticity fixed points in the case of null vorticity diffusion flux normal to the wall

In the local coordinate system (t_1, t_2) tangent to the wall [Fig. 1(B)], let us first consider the case when:

$$\exists \tilde{\boldsymbol{x}} \in \partial\Omega : \sigma_{\boldsymbol{n}} = -\nu(\nabla_{\boldsymbol{\pi}} \cdot \boldsymbol{\omega})_{\tilde{\boldsymbol{x}}} = 0. \tag{17}$$

Reminding from Eq. (12) that all quantities expressing σ_n take value on $\partial\Omega$, it follows that:

$$\forall \tilde{\boldsymbol{x}} \in \partial\Omega : \boldsymbol{\tau}(\tilde{\boldsymbol{x}}) = \boldsymbol{\omega}_{\partial\Omega}(\tilde{\boldsymbol{x}}) = 0 \wedge \sigma_{\boldsymbol{n}} = 0 \Rightarrow \frac{\partial\omega_{t_1}}{\partial t_1} = -\frac{\partial\omega_{t_2}}{\partial t_2}. \tag{18}$$

According to Eq. (14), the characteristic polynomial of the Jacobian matrix of $\boldsymbol{\tau}$ at $\tilde{\boldsymbol{x}} \in \partial\Omega$ can be expressed as:

$$p_{J(\tau)_{\tilde{x}}}(\lambda) = \lambda^2 - \mathrm{tr}\big(J(\boldsymbol{\tau})_{\tilde{\boldsymbol{x}}}\big)\lambda + \det\big(J(\boldsymbol{\tau})_{\tilde{\boldsymbol{x}}}\big) = 0, \tag{19}$$

where $J(\boldsymbol{\tau})_{\tilde{\boldsymbol{x}}}$, from Eq. (15), assumes the following expression:

$$\mathrm{J}(\tau)_{\tilde{\mathrm{x}}} = \begin{pmatrix} \frac{\partial\tau_{t_1}}{\partial t_1} & \frac{\partial\tau_{t_1}}{\partial t_2} \\ \frac{\partial\tau_{t_2}}{\partial t_1} & \frac{\partial\tau_{t_2}}{\partial t_2} \end{pmatrix}_{\tilde{\mathrm{x}}} = \mu\begin{pmatrix} \frac{\partial\omega_{t_2}}{\partial t_1} & \frac{\partial\omega_{t_2}}{\partial t_2} \\ -\frac{\partial\omega_{t_1}}{\partial t_1} & -\frac{\partial\omega_{t_1}}{\partial t_2} \end{pmatrix}_{\tilde{\mathrm{x}}}. \tag{20}$$

Hence, in the case of $\sigma_n = 0$, the Jacobian matrix $J(\boldsymbol{\tau})_{\tilde{\boldsymbol{x}}}$ must be symmetric because of Eq. (18).

Similarly, considering the mathematical restriction on the trace of the Jacobian matrix of $\boldsymbol{\omega}_{\partial\Omega}$, i.e., $\mathrm{tr}\big(J(\boldsymbol{\omega}_{\partial\Omega})_{\tilde{\boldsymbol{x}}}\big) = (\nabla \cdot \boldsymbol{\omega}_{\partial\Omega}) = (\nabla_\pi \cdot \boldsymbol{\omega}) = 0$, the characteristic polynomial $p_{J(\omega_{\partial\Omega})_{\tilde{x}}}$ calculated at the fixed point $\tilde{\boldsymbol{x}} \in \partial\Omega$ can be expressed as:

$$p_{J(\boldsymbol{\omega}_{\partial\Omega})_{\tilde{\boldsymbol{x}}}} = \lambda^2 + \det\big(J(\boldsymbol{\omega}_{\partial\Omega})_{\tilde{\boldsymbol{x}}}\big) = 0. \tag{21}$$

Considering Eqs. (18) and (20), we have that $\det(J(\boldsymbol{\omega}_{\partial\Omega})) = \frac{\det(J(\boldsymbol{\tau}))}{\mu^2}$, and since $\det(J) = \lambda_1\lambda_2$, from Eqs. (20) and (21) the following conditions emerge:

- if $\det(J(\boldsymbol{\omega}_{\partial\Omega})_{\tilde{\boldsymbol{x}}}) = \frac{\det(J(\boldsymbol{\tau})_{\tilde{\boldsymbol{x}}})}{\mu^2} < 0$, then eigenvalues λ_1 and λ_2 are real numbers with opposite sign, indicating that $\tilde{\boldsymbol{x}}$ is a saddle point for both $\boldsymbol{\omega}_{\partial\Omega}$ and $\boldsymbol{\tau}$ [Table I, Fig. 3(A)];
- if $\det(J(\boldsymbol{\omega}_{\partial\Omega})_{\tilde{\boldsymbol{x}}}) = \frac{\det(J(\boldsymbol{\tau})_{\tilde{\boldsymbol{x}}})}{\mu^2} > 0$, then eigenvalues λ_1 and λ_2 are pure imaginary numbers for $\boldsymbol{\omega}_{\partial\Omega}$ and real numbers with the same sign for $\boldsymbol{\tau}$ (due to the symmetry of the Jacobian matrix

of $\boldsymbol{\tau}$). Hence, the fixed point $\tilde{\boldsymbol{x}}$ is a center for $\boldsymbol{\omega}_{\partial\Omega}$ (Table I, Fig. 3) and can be a node (if $\det\left(J(\boldsymbol{\omega}_{\partial\Omega})_{\tilde{\boldsymbol{x}}}\right) < \frac{\mathrm{tr}^2\left(J(\boldsymbol{\omega}_{\partial\Omega})_{\tilde{\boldsymbol{x}}}\right)}{4}$) or a star node (if $\left(\det\left(J(\boldsymbol{\omega}_{\partial\Omega})_{\tilde{\boldsymbol{x}}}\right) = \frac{\mathrm{tr}^2\left(J(\boldsymbol{\omega}_{\partial\Omega})_{\tilde{\boldsymbol{x}}}\right)}{4}\right)$ for $\boldsymbol{\tau}$ [Table I, Fig. 3(A)].

Moreover, if $\sigma_n = 0$ at the fixed point $\tilde{\boldsymbol{x}}$, then the Jacobian matrix of $\boldsymbol{\tau}$ will be characterized by orthogonal eigenvectors, due to its symmetry.

The possible combinations of the nature of the fixed point $\tilde{\boldsymbol{x}} \in \partial\Omega$ for wall shear stress and surface vorticity, when Eq. (17) is satisfied, are summarized in Fig. 3(A).

2. Wall shear stress and surface vorticity fixed points in the case of not-null vorticity diffusion flux normal to the wall

In the same local coordinate system (t_1, t_2) as shown in Fig. 1(B), we now consider the case where a not-null vorticity diffusion flux normal to the wall is established, i.e.:

$$\exists\, \hat{\boldsymbol{x}} \in \partial\Omega \,:\, \sigma_n = -\nu\left(\nabla_{\boldsymbol{\pi}} \cdot \boldsymbol{\omega}\right)_{\hat{\boldsymbol{x}}} \neq 0. \tag{22}$$

From Eq. (12), and always keeping in mind that all quantities expressing σ_n take value on $\partial\Omega$, in the case Eq. (22) is satisfied, it follows that:

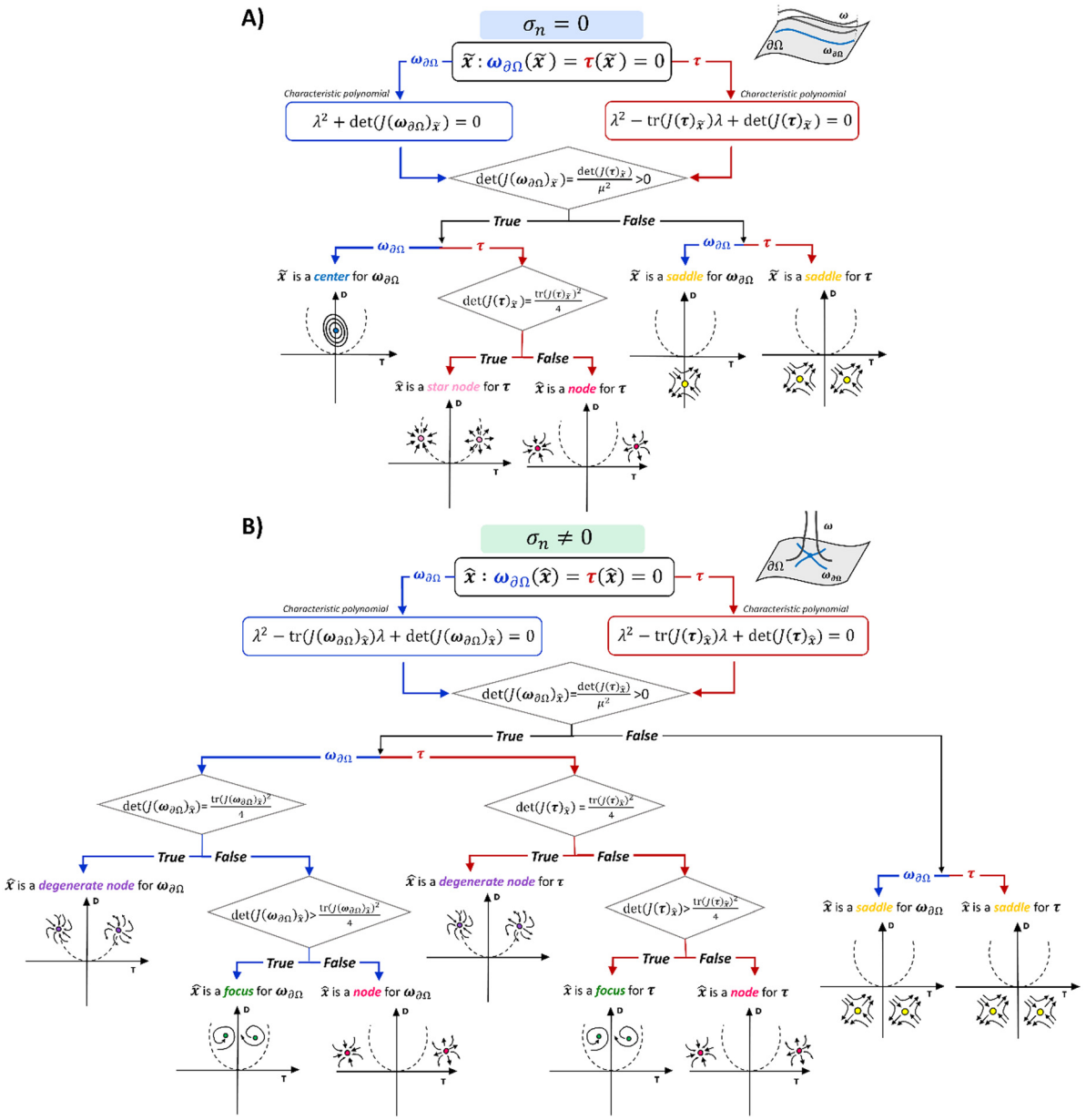

FIG. 3. Chart of the analysis of wall shear stress and surface vorticity fixed points in the case of (A) null vorticity diffusion flux normal to the wall and (B) not-null vorticity diffusion flux normal to the wall.

$$\forall \hat{\boldsymbol{x}} \in \partial\Omega : \boldsymbol{\tau}(\hat{\boldsymbol{x}}) = \boldsymbol{\omega}_{\partial\Omega}(\hat{\boldsymbol{x}}) = 0 \wedge \sigma_n \neq 0 \Rightarrow \frac{\partial}{\partial n}(\boldsymbol{\omega}\cdot\boldsymbol{n}) = -\frac{\partial \omega_{t_1}}{\partial t_1} - \frac{\partial \omega_{t_2}}{\partial t_2} \neq 0. \tag{23}$$

The classification of the nature of $\boldsymbol{\tau}$ and $\boldsymbol{\omega}_{\partial\Omega}$ fixed points $\hat{\boldsymbol{x}} \in \partial\Omega$ can be performed, as previously done, by solving the characteristic polynomials of the Jacobian matrices of $\boldsymbol{\tau}$ and $\boldsymbol{\omega}_{\partial\Omega}$ at $\hat{\boldsymbol{x}}$, and analyzing the eigenvalues λ_i associated with them:

$$\mathrm{p}_{J(\boldsymbol{\tau})_{\hat{\boldsymbol{x}}}}(\lambda) = \lambda^2 - \mathrm{tr}\left(J(\boldsymbol{\tau})_{\hat{\boldsymbol{x}}}\right)\lambda + \det\left(J(\boldsymbol{\tau})_{\hat{\boldsymbol{x}}}\right) = 0, \tag{24}$$

$$p_{J(\boldsymbol{\omega}_{\partial\Omega})_{\hat{\boldsymbol{x}}}}(\lambda) = \lambda^2 - \mathrm{tr}\left(J(\boldsymbol{\omega}_{\partial\Omega})_{\hat{\boldsymbol{x}}}\right)\lambda + \det\left(J(\boldsymbol{\omega}_{\partial\Omega})_{\hat{\boldsymbol{x}}}\right) = 0. \tag{25}$$

From Eq. (24), a consequence of having $\sigma_n(\hat{\boldsymbol{x}}) \neq 0$ is that $J(\boldsymbol{\tau})_{\hat{\boldsymbol{x}}}$ is no longer symmetric, since $\frac{\partial \omega_{t_2}}{\partial t_2} + \frac{\partial \omega_{t_1}}{\partial t_1} = \nabla_\pi \cdot \boldsymbol{\omega} \neq 0$ [as evident from Eq. (20), which has a general form]. Therefore, the consequences for $\sigma_n(\hat{\boldsymbol{x}}) \neq 0$ are that:

- if $\det(J(\boldsymbol{\omega}_{\partial\Omega})_{\hat{\boldsymbol{x}}}) = \frac{\det(J(\boldsymbol{\tau})_{\hat{\boldsymbol{x}}})}{\mu^2} < 0$, then eigenvalues λ_1 and λ_2 are real numbers with opposite sign, indicating that $\hat{\boldsymbol{x}}$ is a saddle point for both $\boldsymbol{\omega}_{\partial\Omega}$ and $\boldsymbol{\tau}$ [Table I, Fig. 3(B)];
- if $\det(J(\boldsymbol{\omega}_{\partial\Omega})_{\hat{\boldsymbol{x}}}) = \frac{\det(J(\boldsymbol{\tau})_{\hat{\boldsymbol{x}}})}{\mu^2} > 0$, then eigenvalues λ_1 and λ_2 may either be complex conjugate, or real numbers with the same sign, indicating that $\hat{\boldsymbol{x}}$ could be a focus, node or degenerate node for both $\boldsymbol{\omega}_{\partial\Omega}$ and $\boldsymbol{\tau}$, depending on the sign of $\mathrm{tr}\left(J(\boldsymbol{\omega}_{\partial\Omega})_{\hat{\boldsymbol{x}}}\right)^2 - 4\det\left(J(\boldsymbol{\omega}_{\partial\Omega})_{\hat{\boldsymbol{x}}}\right)$ for $\boldsymbol{\omega}_{\partial\Omega}$ and $\mathrm{tr}\left(J(\boldsymbol{\tau})_{\hat{\boldsymbol{x}}}\right)^2 - 4\det\left(J(\boldsymbol{\tau})_{\hat{\boldsymbol{x}}}\right)$ for $\boldsymbol{\tau}$ [Table I, Fig. 3(B)].

In the case where $\sigma_n \neq 0$, the matrix $J(\boldsymbol{\tau})_{\hat{\boldsymbol{x}}}$ cannot be symmetric, implying that $J(\boldsymbol{\tau})_{\hat{\boldsymbol{x}}}$ has non-orthogonal eigenvectors. The possible combinations of the nature of the fixed point $\tilde{\boldsymbol{x}} \in \partial\Omega$ for wall shear stress and surface vorticity, when Eq. (22) is satisfied, are summarized in Fig. 3(B).

C. Computational hemodynamics

As in our previous study,[45] intracranial aneurysm models from the Toronto Western Hospital aneurysm clinic were used to test results from the theoretical analysis. These cases were provided under Toronto Western Hospital's Research Ethics Board Approval (REB #19–5823), which permits the research analysis and publication of anonymized and de-identified patient imaging data from their aneurysm clinic. The geometry reconstruction, meshing strategy, and CFD settings have been extensively described in prior studies.[15,45,55,56]

The identification and classification of fixed points on the luminal surface of intracranial aneurysm models are performed by computing the Poincaré index and the eigenvalues of the Jacobian matrix J as detailed in previous studies.[15] In line with the previous study,[45] a characterization of the intricate velocity and vorticity structures in the intracranial aneurysm models was conducted to identify the hemodynamic features that interacting with the vessel wall $\partial\Omega$ determine the topology of wall shear stress and surface vorticity fields. To achieve this, the recently proposed vorticity vector decomposition into a purely rotational contribution $\boldsymbol{R}$, representing the rigid-body rotation, and a non-rotational contribution associated with shear, was adopted.[57,58] For the basic theory underlying this vorticity vector decomposition, the reader is referred to Refs. 57, 59, and 60. Here, we focus on the rotational part $\boldsymbol{R}$ of the vorticity, which can be defined as:[59]

$$\boldsymbol{R} = Rr = \left(\boldsymbol{\omega}\cdot\boldsymbol{r} - \sqrt{(\boldsymbol{\omega}\cdot\boldsymbol{r})^2 - 4\lambda_{ci}^2}\right)\boldsymbol{r}, \tag{26}$$

where R is local rotation strength, $\boldsymbol{r}$ is the unit real eigenvector of the velocity gradient tensor $\nabla\boldsymbol{u}$, and λ_{ci} is the imaginary part of the complex conjugate eigenvalues of $\nabla\boldsymbol{u}$. Unlike other vortex identification methods such as Q-criterion, λ_2 or λ_{ci}, $\boldsymbol{R}$ provides both the vortex local rotational axis and the rotational strength, free from shear contamination.[61]

III. RESULTS

A. Wall shear stress and surface vorticity fixed points

Two illustrative configurations of surface vorticity and wall shear stress patterns are presented in Fig. 4, highlighting the potential mutual relationships between their fixed points in terms of nature and stability properties. Specifically, the visualizations in Fig. 4 confirm that, regardless of whether σ_n is zero or non-zero: (i) $\boldsymbol{\tau}$ and $\boldsymbol{\omega}_{\partial\Omega}$ form an orthogonal pair on the luminal surface $\partial\Omega$; (ii) fixed points for $\boldsymbol{\omega}_{\partial\Omega}$ are always fixed points for $\boldsymbol{\tau}$, and vice versa; (iii) $\boldsymbol{\tau}$ and $\boldsymbol{\omega}_{\partial\Omega}$ may exhibit different topological skeletons on the luminal surface, in accordance with the developed theory summarized in Fig. 3. More specifically, Fig. 4(A) presents the case of two fixed points, both of which are saddle points for $\boldsymbol{\omega}_{\partial\Omega}$ and $\boldsymbol{\tau}$, and the case of one fixed point that is a center for $\boldsymbol{\omega}_{\partial\Omega}$ and an unstable star node for $\boldsymbol{\tau}$. The allowed combinations for wall shear stress and surface vorticity fixed points of Fig. 4(A) illustrate the case of a local null vorticity diffusion flux normal to the wall, in the near-wall region. Alternative combinations of fixed points allowed for the case where σ_n is not-null include the stable focus-stable focus pair and, again, the saddle point-saddle point pair for $\boldsymbol{\omega}_{\partial\Omega}$ and $\boldsymbol{\tau}$, as shown in Fig. 4(B).

The visualizations of $\boldsymbol{\tau}$ and $\boldsymbol{\omega}_{\partial\Omega}$ patterns on the luminal surface of the two illustrative intracranial aneurysm CFD models presented in Fig. 5 (model A1) and in Fig. 6 (model A2), confirm that the locations of the fixed points are always identical for both $\boldsymbol{\tau}$ and $\boldsymbol{\omega}_{\partial\Omega}$. Furthermore, Figs. 5 and 6 demonstrate that at the same location, the fixed point for $\boldsymbol{\tau}$ can have different nature and stability properties compared to the fixed point for $\boldsymbol{\omega}_{\partial\Omega}$, resulting in different topological skeletons for surface vorticity and wall shear stress. Specifically, for model A1, topological configurations consistent with the theory are observed: three saddle points for both $\boldsymbol{\tau}$ and $\boldsymbol{\omega}_{\partial\Omega}$, one unstable node for $\boldsymbol{\tau}$ that is a center for $\boldsymbol{\omega}_{\partial\Omega}$, one stable focus for both $\boldsymbol{\tau}$ and $\boldsymbol{\omega}_{\partial\Omega}$, and one unstable star node for $\boldsymbol{\tau}$ that is a center for $\boldsymbol{\omega}_{\partial\Omega}$ (Fig. 5). The unstable and stable manifolds connected to a saddle point for $\boldsymbol{\tau}$ [i.e., the critical lines attracting and repelling neighboring fluid elements, as shown in Fig. 2(A)] are rotated with respect to the unstable and stable manifolds connected to the saddle point for $\boldsymbol{\omega}_{\partial\Omega}$ [Figs. 5(A)–5(C)]. Additionally, it can be appreciated that the diverging wall shear stress pattern around both an unstable node [Fig. 5(A)] and an unstable star node for $\boldsymbol{\tau}$ [Fig. 5(C)] colocalizes with $\boldsymbol{\omega}_{\partial\Omega}$ field lines forming a closed loop enclosing the center for $\boldsymbol{\omega}_{\partial\Omega}$ [Figs. 5(A) and 5(C)]. Moreover, where a stable focus for both $\boldsymbol{\tau}$ and $\boldsymbol{\omega}_{\partial\Omega}$ is identified, spiral-shaped counter-rotating field lines characterize the two topological skeletons in the neighborhood [Fig. 5(A)].

The analysis of model A2 (Fig. 6) confirms that the simulated data are aligned with theoretical expectations. Specifically, for model A2 two fixed points are identified that are saddle points for both $\boldsymbol{\tau}$ and $\boldsymbol{\omega}_{\partial\Omega}$, one unstable node for $\boldsymbol{\tau}$ that is a stable focus for $\boldsymbol{\omega}_{\partial\Omega}$, and one stable focus for $\boldsymbol{\tau}$ that is an unstable focus for $\boldsymbol{\omega}_{\partial\Omega}$, on the luminal

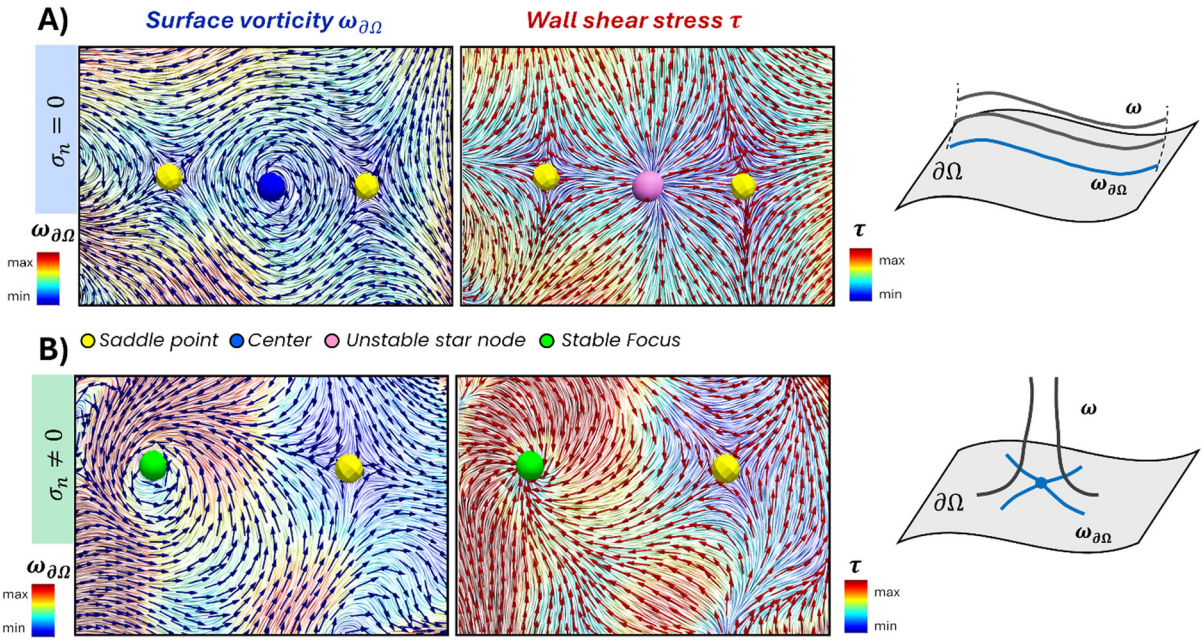

FIG. 4. (A) Explanatory configurations of surface vorticity and wall shear stress topological skeletons with their fixed points (saddle points for both surface vorticity and wall shear stress; center for surface vorticity which is an unstable star node for wall shear stress) in case the vorticity diffusion flux normal to the wall has a null value; (B) explanatory configurations of surface vorticity and wall shear stress with their fixed points (stable focus and saddle point for both surface vorticity and wall shear stress in case the vorticity diffusion flux normal to the wall has a not-null value.

surface of the aneurysmal sac (Fig. 6). Contrarily to model A1, around the fixed point identified as unstable node for $\boldsymbol{\tau}$ and stable focus for $\boldsymbol{\omega}_{\partial\Omega}$, the source configuration of the $\boldsymbol{\tau}$ field lines colocalizes with the converging spiral-shaped $\boldsymbol{\omega}_{\partial\Omega}$ field lines (Fig. 6). This configuration is linked to the existence of a local net vorticity diffusion flux σ_n normal to the wall, ensuring that the underlying theory is not violated.

B. Identifying the link between fixed points and intravascular fluid structures

An atlas of the allowed combinations of fixed points for wall shear stress and surface vorticity, their associated local field topologies on the luminal surface, and the corresponding flow patterns near the wall is presented in Fig. 7. These visualizations include instantaneous velocity streamlines, vortex lines and the rotational part of vorticity $\boldsymbol{R}$ [as introduced in Eq. (26)]. In general, depending on the possible combinations of nature and stability for wall shear stress and surface vorticity fixed points, either rotational or non-rotational fluid structures can interact with the wall, impinging upon or emanating from it. These fluid structures may or may not be associated with the existence of a local net vorticity diffusion flux normal to the wall, in the near-wall region and under the action of blood currents may extend further into the aneurysmal dome. Specifically, Fig. 7(A) illustrates the case where the vorticity diffusion flux normal to the wall is null ($\sigma_n = 0$). In such a scenario, a fixed point that is a saddle point for both $\boldsymbol{\tau}$ and $\boldsymbol{\omega}_{\partial\Omega}$ attracts and repels velocity field lines in the near-wall region (as highlighted by the visualization of instantaneous velocity streamlines that remain parallel to the wall in this region), while no vortex lines extensions into the aneurysmal dome are observed near the location of the fixed point [Fig. 7(A)]. It can be also observed that the unstable and stable manifolds connected to a saddle point for $\boldsymbol{\tau}$ are orthogonal, due to the symmetry of $J(\boldsymbol{\tau})_{\hat{\boldsymbol{x}}}$ when $\sigma_n = 0$ [see Eqs. (18) and (20)]. Furthermore, in a scenario where $\sigma_n = 0$, the near-wall hemodynamics around an unstable star node for $\boldsymbol{\tau}$, which is also a center for $\boldsymbol{\omega}_{\partial\Omega}$, is characterized by circularly shaped vortex lines lying on the wall and by a non-rotational fluid structure with a velocity normal component impinging on the wall [Fig. 7(A)], physically consistent with the diverging wall shear stress straight field lines pattern around the fixed point.

Figure 7(B) illustrates the case $\sigma_n \neq 0$. In such a scenario: (i) a saddle point for both $\boldsymbol{\tau}$ and $\boldsymbol{\omega}_{\partial\Omega}$ is associated with the presence of two counter-rotating fluid structures in the near-wall region, highlighted by the R isosurfaces visualization. In a case like this, the local topological skeletons for $\boldsymbol{\tau}$ and $\boldsymbol{\omega}_{\partial\Omega}$ are the result of the complex near-wall fluid dynamics, with velocity and vortex lines exhibiting not-null, oppositely oriented components normal to the wall [Fig. 7(B)]; (ii) a fixed point that is a stable focus for both $\boldsymbol{\tau}$ and $\boldsymbol{\omega}_{\partial\Omega}$ is encased by spiral-shaped $\boldsymbol{\tau}$ and $\boldsymbol{\omega}_{\partial\Omega}$ field lines, and is associated with a near-wall rotational fluid structure characterized by a local velocity field with a component normal to the wall, as well as with vortex lines emanating from the wall [Fig. 7(B)]; (iii) an unstable node for $\boldsymbol{\tau}$ that is a stable focus for $\boldsymbol{\omega}_{\partial\Omega}$ is associated with a non-rotational near-wall fluid structure (highlighted by the R isosurfaces visualization), where local velocity and vortex lines exhibit oppositely oriented components normal to the wall. In a case like this, the topological skeleton for $\boldsymbol{\omega}_{\partial\Omega}$ features spiral-shaped field lines encasing the fixed point, while the local field topology for $\boldsymbol{\tau}$ resembles the near-wall tangent velocity field lines [Fig. 7(B)]; (iv) a fixed point that is a stable focus for $\boldsymbol{\tau}$ and a stable

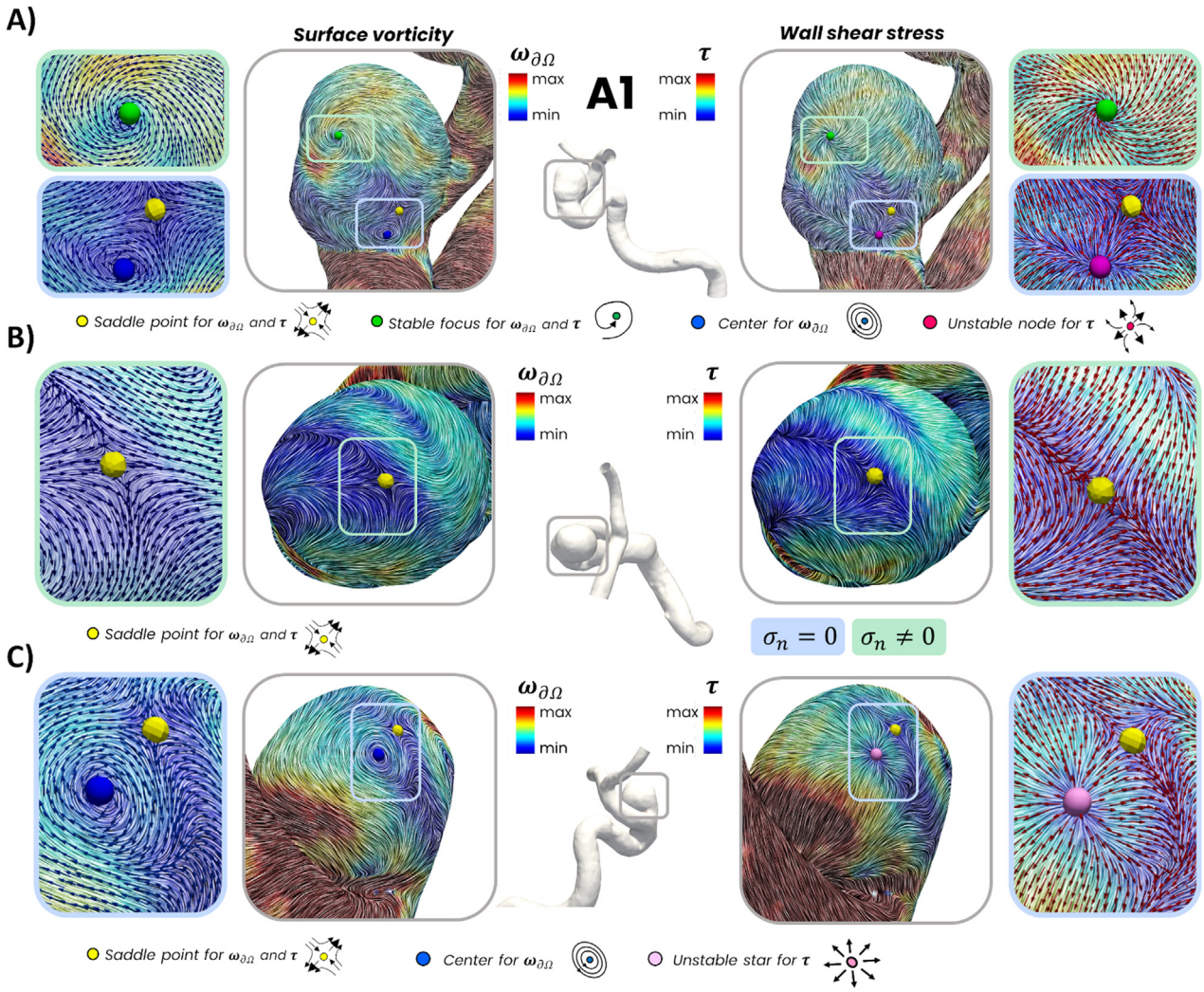

FIG. 5. Visualization of instantaneous surface vorticity (left panel) and wall shear stress (right panel) field lines and vector fields on the luminal surface of intracranial aneurysm model A1. Flow visualizations refer to mid acceleration phase in systole. Surface vorticity and wall shear stress fixed points are depicted. Three different views are displayed: (A) front view, (B) top view, and (C) back view. Four insets zooming on fixed points locations are displayed to appreciate the field topology in their neighborhood.

node for $\omega_{\partial\Omega}$ is the result of the presence of a fluid structure characterized by rotational velocity field lines and vorticity field lines, both of them presenting with a normal component emanating from the wall [Fig. 7(B)].

According to the theoretical framework in Fig. 3, Fig. 8 clearly demonstrates that a fixed point for wall shear stress and surface vorticity can exhibit different natures. The explanatory example in Fig. 8(A) clarifies that a center for $\omega_{\partial\Omega}$, characterized by circularly shaped vortex lines, can correspond to either an unstable node or an unstable star node for τ. In both cases, the fixed point is associated with a non-rotational fluid structure impinging on the wall, but the local topological skeleton encasing the fixed point differs: diverging, not straight field lines where τ is an unstable node and diverging, straight field lines where τ is an unstable star node. Similarly, the explanatory example in Fig. 8(B) shows that a stable focus for $\omega_{\partial\Omega}$, characterized by spiral-shaped vortex lines emanating from the wall in the near-wall region, can manifest as a stable focus or a stable degenerate node for τ: the former is associated with a rotational fluid structure impinging on the wall, the latter with a non-rotational one.

IV. DISCUSSION

The unified theory presented in our previous study[45] is revised and expanded here with the ultimate goal of demonstrating that the topological skeleton of wall shear stress on the luminal surface of a vessel is "sculpted" by distinct intravascular fluid structures in the near-wall region.

Before summarizing the study's main findings, it is important to interpret the theoretical link established by Eq. (9) in the context of the physics of fluids. The topological skeletons for wall shear stress and surface vorticity reflect the distinctive characteristics of the near-wall

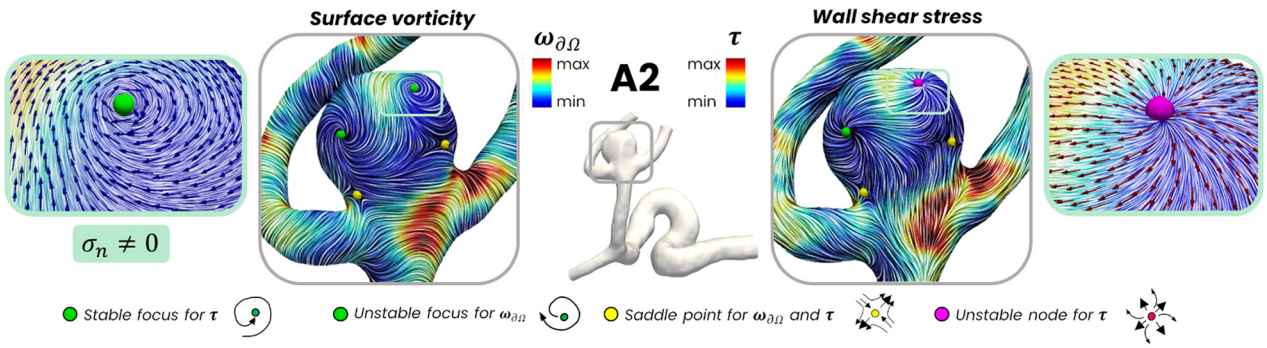

FIG. 6. Visualization of instantaneous surface vorticity (left panel) and wall shear stress (right panel) field lines and vector fields on the luminal surface of intracranial aneurysm model A2. Flow visualizations refer to mid acceleration phase in systole. Surface vorticity and wall shear stress fixed points are depicted. One inset zooming on fixed points locations is displayed to appreciate the field topology in their neighborhood.

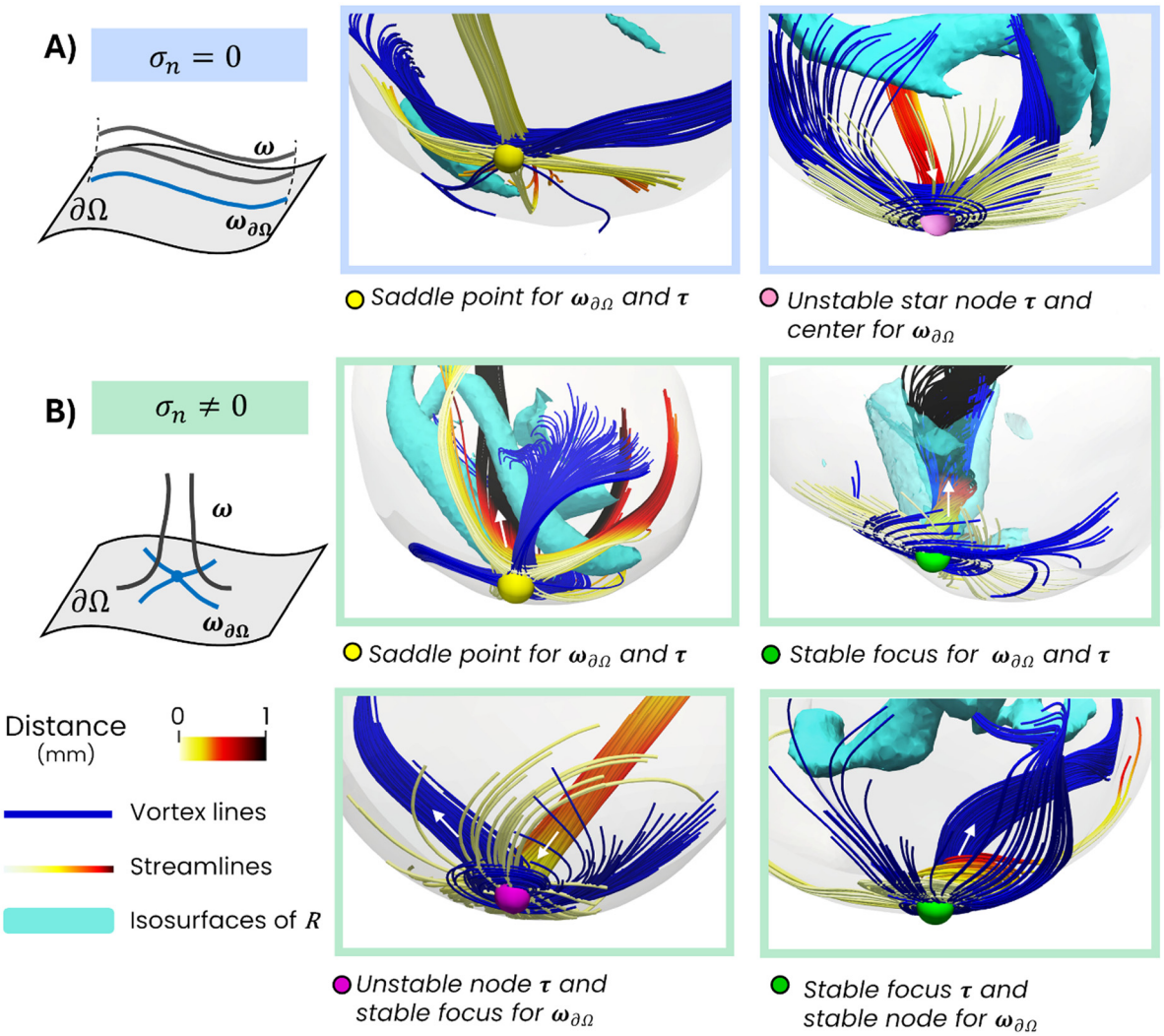

FIG. 7. Explanatory configurations of velocity streamlines, vortex lines, and R isosurfaces around wall shear stress and surface vorticity fixed points (A) in the case the vorticity diffusion flux normal to the wall has null value, and (B) in the case the vorticity diffusion flux normal to the wall has a not-null value. White arrows indicate the direction of velocity streamlines and vortex lines. Velocity streamlines are colored with the distance from the luminal surface, to highlight how much there are lengthened inside the aneurysmal dome by blood flow drafts.

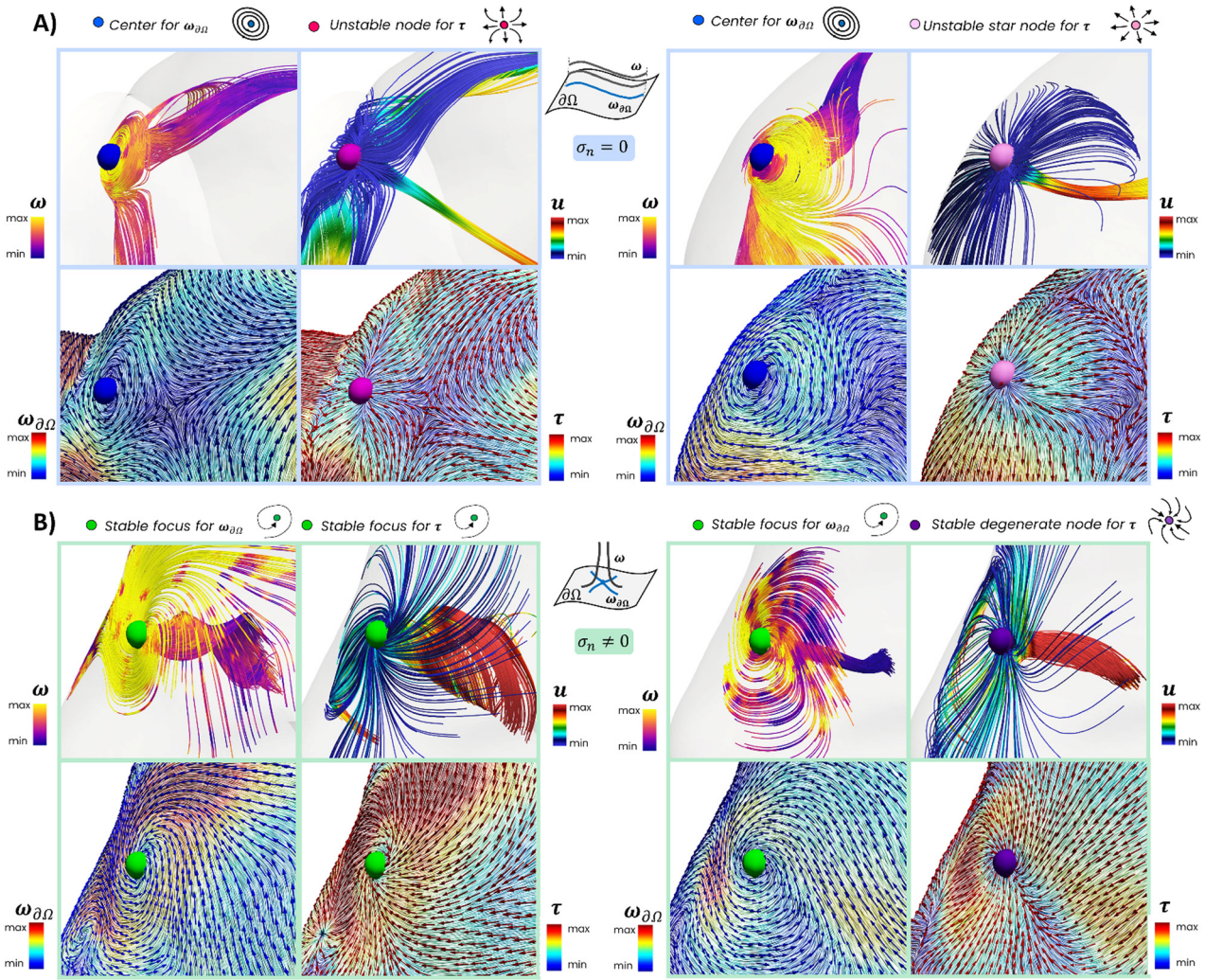

FIG. 8. Explanatory configurations of vortex lines, velocity streamlines, surface vorticity, and wall shear stress vector fields around wall shear stress and surface vorticity fixed points to highlight the multiple nature of fixed points (A) in the case the vorticity diffusion flux normal to the wall has null value (a center for surface vorticity can be an unstable node or an unstable star node for wall shear stress), and (B) in the case the vorticity diffusion flux normal to the wall has a not-null value (a stable focus for surface vorticity can be a stable focus or stable degenerate node for wall shear stress).

fluid structures interacting with a material surface: the topological skeleton around a fixed point for wall shear stress mirrors the near-wall tangent velocity field,[49] while for surface vorticity, it represents the imprint of the local vorticity kinematics on the wall. Furthermore, Eq. (9) reveals that the manifolds of wall shear stress and vorticity undergo mutual rotation. Consequently, their topological skeletons around a fixed point may appear similar or distinct, a relationship that the theory can predict with precision.

In our previous article,[45] the theoretical discussion on the relationship between wall shear stress and surface vorticity fixed points considered a scenario where the normal component of the surface vorticity could be not null. However, surface vorticity must remain tangent to a material surface if the velocity obeys the no-slip condition [i.e., Eq (11) is always satisfied]. This led us to the erroneous conclusion that, in certain cases, a fixed point for wall shear stress may not be a fixed point for surface vorticity, an interpretation that violates Eq. (11), which is always satisfied.[45] Since the opportunity to correct this erroneous interpretation was denied, in this study we have partially revised the previous theory, clarifying that all fixed points of wall shear stress must also be fixed points of surface vorticity, and vice versa. Furthermore, we reinforced the analysis by demonstrating that the nature and stability of a fixed point are not necessarily identical for surface vorticity and wall shear stress. In addition, we expanded the theoretical framework by incorporating a more comprehensive classification of fixed points, and we constructed an atlas of all the possible combinations of near-wall velocity and vorticity structures associated with wall shear stress and surface vorticity topological skeletons around their fixed points.

Combination of WSS and SV fixed points		Local near-wall fluid structures	
WSS fixed point	SV fixed point	Vorticity	Velocity
$\sigma_n = 0$			
Stable star node (with orthogonal eigenvectors)	Center	Vortex lines parallel to the wall	Non-rotational fluid structure velocity with normal component emanating from the wall
Unstable star node (with orthogonal eigenvectors)	Center		Non-rotational fluid structure velocity with normal component impinging to the vessel wall
Stable node (with orthogonal eigenvectors)	Center		Non-rotational fluid structure velocity with normal component emanating from the wall
Unstable node (with orthogonal eigenvectors)	Center		Non-rotational fluid structure velocity with normal component impinging to the vessel wall
Saddle (with orthogonal eigenvectors)	Saddle		Velocity field parallel from the wall

FIG. 9. Summary of the nature of the theoretically admitted relationships between wall shear stress fixed points, surface vorticity fixed points, and near-wall flow fluid structures in terms of vorticity and velocity in the case of null vorticity diffusion flux normal to the wall.

The taxonomy summarizing the main findings of this study is presented in Figs. 9 and 10. Specifically, for each permissible combination of wall shear stress and surface vorticity fixed points, when the vorticity diffusion flux normal to the wall is null ($\sigma_n = 0$), the characteristics of the associated near-wall fluid structures are detailed in Fig. 9: (i) a stable/unstable node for wall shear stress always corresponds to a center for surface vorticity. This fixed point is associated with a non-rotational fluid structure, characterized by near-wall velocity emanating from or impinging on the wall. This interaction shapes the wall shear stress skeleton with converging or diverging field lines (where the eigenvectors of the wall shear stress Jacobian matrix are orthogonal) and the surface vorticity skeleton with circular lines, around the fixed point; (ii) if the stable/unstable node for wall shear stress described in the previous point is a star node, its skeleton is defined by converging or diverging straight field lines, a consequence of the wall shear stress Jacobian matrix being proportional to the identity matrix in this case; (iii) a saddle point for wall shear stress always corresponds to a saddle point for surface vorticity (and vice versa). This fixed point involves near-wall kinematics where velocity and vortex lines are parallel to the wall, shaping the two topological skeletons with converging and diverging patterns along principal directions, which are mutually oriented according to Eq. (9). For each permissible combination of wall shear stress and surface vorticity fixed points, when the vorticity diffusion flux normal to the wall is not null ($\sigma_n \neq 0$), the characteristics of the associated near-wall fluid structures are detailed in Fig. 10: (i) a stable/unstable node for wall shear stress can correspond to a stable/unstable node, a degenerate node (with local topology characterized by converging/diverging field lines), or a stable/unstable focus (with topology characterized by spiral-shaped field lines) for surface vorticity. This fixed point is associated with a non-rotational fluid structure characterized by near-wall velocity emanating from/impinging on the wall, which shapes the wall shear stress skeleton in terms of converging/diverging field lines (in this case the eigenvectors of the wall shear stress Jacobian matrix are non-orthogonal), and vortex lines emanating from/impinging on the wall; (ii) if the stable/unstable node for wall shear stress described above is a degenerate node, the latter attracts/repels wall shear stress field lines collapsing along a principal direction; (iii) a stable/unstable focus for wall shear stress can correspond to a stable/unstable node, a degenerate node, or a stable/unstable focus for surface vorticity. This fixed point is always associated with a rotational fluid structure characterized by near-wall velocity emanating from/impinging on the wall, which shapes wall shear stress in terms of spiral field lines [due to the presence of a net vorticity diffusion flux normal to the wall, that can be expressed in terms of curl of the wall shear stress, see Eq. (13)]; (iv) a saddle point for wall shear stress always corresponds to a saddle point for surface vorticity (and vice versa). This fixed point involves near-wall dynamics where velocity and vortex lines oppositely emanate from and impinge on the wall.

The stability or instability of a wall shear stress (surface vorticity) focus or node is intrinsically connected to near-wall dynamics, which is characterized by velocity lines (vortex lines) either emanating from or impinging on the wall. However, only a stable/unstable focus for wall shear stress is consistently associated with a near-wall dynamics where rotational velocity and vorticity lines emanate from or impinge on the wall.

High-fidelity CFD data from intracranial aneurysm models confirmed the theoretical links between wall shear stress and surface vorticity topology on the luminal surface.

Among the main fluid mechanical implications, the proposed analysis establishes a clear and direct link between the topological skeletons of wall shear stress and surface vorticity, shaped by the interaction between the material surface and near-wall fluid dynamics. In cardiovascular flows, this cross-data topological analysis holds

Combination of WSS and SV fixed points		Local near-wall fluid structures	
WSS fixed point	**SV fixed point**	**Vorticity**	**Velocity**
$\sigma_n \neq 0$			
Stable degenerate node 	Stable degenerate node	Vortex lines emanating from the wall	 Non-rotational fluid structure *velocity with normal component emanating from the wall*
	Unstable degenerate node	Vortex lines impinging on the wall	
	Stable node	Vortex lines emanating from the wall	
	Unstable node	Vortex lines impinging on the wall	
	Stable focus	Vortex lines emanating from the wall	
	Unstable focus	Vortex lines impinging on the wall	
Unstable degenerate node 	Stable degenerate node	Vortex lines emanating from the wall	 Non-rotational fluid structure *velocity with normal component impinging on the wall*
	Unstable degenerate node	Vortex lines impinging on the wall	
	Stable node	Vortex lines emanating from the wall	
	Unstable node	Vortex lines impinging on the wall	
	Stable focus	Vortex lines emanating from the wall	
	Unstable focus	Vortex lines impinging on the wall	
Stable node  (with non-orthogonal eigenvectors)	Stable degenerate node	Vortex lines emanating from the wall	 Non-rotational fluid structure *velocity with normal component emanating from the wall*
	Unstable degenerate node	Vortex lines impinging on the wall	
	Stable node	Vortex lines emanating from the wall	
	Unstable node	Vortex lines impinging on the wall	
	Stable focus	Vortex lines emanating from the wall	
	Unstable focus	Vortex lines impinging on the wall	
Unstable node  (with non-orthogonal eigenvectors)	Stable degenerate node	Vortex lines emanating from the wall	 Non-rotational fluid structure *velocity with normal component impinging on the wall*
	Unstable degenerate node	Vortex lines impinging on the wall	
	Stable node	Vortex lines emanating from the wall	
	Unstable node	Vortex lines impinging on the wall	
	Stable focus	Vortex lines emanating from the wall	
	Unstable focus	Vortex lines impinging on the wall	
Stable focus 	Stable degenerate node	Vortex lines emanating from the wall	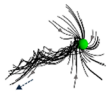 Rotational fluid structure *velocity with normal component emanating from the wall*
	Unstable degenerate node	Vortex lines impinging on the wall	
	Stable node	Vortex lines emanating from the wall	
	Unstable node	Vortex lines impinging on the wall	
	Stable focus	Vortex lines emanating from the wall	
	Unstable focus	Vortex lines impinging on the wall	
Unstable focus 	Stable degenerate node	Vortex lines emanating from the wall	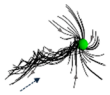 Rotational fluid structure *velocity with normal component impinging on the wall*
	Unstable degenerate node	Vortex lines impinging on the wall	
	Stable node	Vortex lines emanating from the wall	
	Unstable node	Vortex lines impinging on the wall	
	Stable focus	Vortex lines emanating from the wall	
	Unstable focus	Vortex lines impinging on the wall	
Saddle  (with non-orthogonal eigenvectors)	Saddle  (with non-orthogonal eigenvectors)	Velocity and vorticity with components normal to the wall *non-rotational fluid structures and vorticity developing along different directions*	

FIG. 10. Summary of the nature of the theoretically admitted relationships between wall shear stress fixed points, surface vorticity fixed points, and near-wall flow fluid structures in terms of vorticity and velocity in the case of not-null vorticity diffusion flux normal to the wall.

potential mechanobiological relevance. For example, the interaction of the luminal surface with shear flow, as opposed to rotational or non-rotational fluid structures, uniquely influences wall shear stress topology, which has emerged as a predictor of vascular disease.[6,8,21,22] By establishing a theoretical connection between the wall shear stress topological skeleton and distinct fluid structures near the wall, this study enables a more precise definition of flow disturbances, whether associated with a specific pathology or a vessel type.

Moreover, the analysis presented, which considers the kinematics of vorticity in the near-wall region, shows potential as a valuable tool for classifying flow disturbances based on their influence on biochemical transport in this region. This potential is supported by two key observations: (i) the wall shear stress topological skeleton is a critical factor in regulating mass transfer at the interface between blood flow and the arterial wall,[62] and (ii) near-wall vorticity can either enhance or hinder the transport of substances to the arterial wall by affecting advection and diffusion processes, modulating accumulation or depletion of atherogenic particles in the near-wall region.[23,24] The capability to clearly link local wall shear stress and surface vorticity topologies to the near-wall blood dynamics represents a crucial step toward understanding how the vessel wall responds to flow disturbances, whether these disturbances result in injury, inflammation, endothelial dysfunction.

The presented analysis may be limited by the potential sensitivity of the theoretical findings to the numerical settings adopted to perform CFD simulations. Nevertheless, the results from the high-fidelity CFD simulations employed in this study align with the cases predicted by the theory, confirming the feasibility of applying the theoretical findings to computational hemodynamic models. Furthermore, the proposed unified theory applies to Newtonian fluids and is limited to fluids confined by rigid surfaces. However, treating blood as a Newtonian fluid has been identified as a source of second-order effects in patient-specific simulations of cardiovascular flows, and assuming rigid walls avoids introducing additional uncertainties related to wall structure and mechanical behavior.[63] Future studies will extend the here presented theory to non-Newtonian fluids and deformable boundaries, to test their real impact in the context of cardiovascular flows.

V. CONCLUSION

A revised and expanded version of the unified theory recently introduced by the authors[45] provides a critical framework for accurately identifying and interpreting the cause-effect relationships linking the near-wall velocity and vorticity structures with wall shear stress and surface vorticity topology on a material surface. This has paramount relevance for cardiovascular flows, where the material surface is the luminal surface of a vessel. By enabling the precise identification of flow disturbances, the theory offers insights into their mechanistic links with biological adverse events and clinical observations. The findings of this study can inform the design of targeted experiments to investigate how features of the wall shear stress topological skeleton, shaped by various near-wall velocity and vorticity structures, influence vascular mechanobiology.

ACKNOWLEDGMENTS

The author V.M. is supported by the project NODES which has received funding from the MUR – M4C2 1.5 of PNRR funded by the European Union – NextGenerationEU (Grant agreement no. ECS00000036). The authors U.M, D.G. and K.C. acknowledge the support of «ASSOCIATE» project (code 2022L7KK7L) – funded by European Union – Next Generation EU within the PRIN 2022 program (D.D. 104 – 02/02/2022 Ministero dell'Università e della Ricerca).

AUTHOR DECLARATIONS

Conflict of Interest

The authors have no conflicts to disclose.

Author Contributions

Valentina Mazzi: Conceptualization (equal); Data curation (equal); Formal analysis (equal); Investigation (equal); Methodology (equal); Visualization (equal); Writing – original draft (equal); Writing – review & editing (equal). **Diego Gallo:** Conceptualization (equal); Methodology (equal); Writing – original draft (equal); Writing – review & editing (equal). **Karol Calò:** Data curation (equal); Visualization (equal); Writing – review & editing (equal). **David Steinman:** Data curation (equal); Writing – original draft (equal); Writing – review & editing (equal). **Umberto Morbiducci:** Conceptualization (equal); Formal analysis (equal); Investigation (equal); Methodology (equal); Supervision (equal); Writing – original draft (equal); Writing – review & editing (equal).

DATA AVAILABILITY

The data that support the findings of this study are available from the corresponding author upon reasonable request.

APPENDIX: RELATIONSHIP BETWEEN VORTICITY FLUX NORMAL TO THE WALL AND CURL OF WALL SHEAR STRESS

Let us consider the mathematical definition of the curl of wall shear stress in the local coordinate system (t_1, t_2, n)

$$\nabla \times \boldsymbol{\tau} = \det \begin{pmatrix} \boldsymbol{t}_1 & \boldsymbol{t}_2 & \boldsymbol{n} \\ \dfrac{\partial}{\partial \boldsymbol{t}_1} & \dfrac{\partial}{\partial \boldsymbol{t}_2} & \dfrac{\partial}{\partial \boldsymbol{n}} \\ \tau_{t_1} & \tau_{t_2} & 0 \end{pmatrix} = \left(-\frac{\partial \tau_{t_2}}{\partial n}\right)\boldsymbol{t}_1 + \left(\frac{\partial \tau_{t_1}}{\partial n}\right)\boldsymbol{t}_2 + \left(\frac{\partial \tau_{t_2}}{\partial t_1} - \frac{\partial \tau_{t_1}}{\partial t_2}\right)\boldsymbol{n}. \quad \text{(A1)}$$

Considering that the wall shear stress lies solely on the surface $\partial\Omega$ (i.e., $\frac{\partial \tau_{t_2}}{\partial n} = \frac{\partial \tau_{t_1}}{\partial n} = 0$), it follows that $\nabla \times \boldsymbol{\tau} = \left(\frac{\partial \tau_{t_2}}{\partial t_1} - \frac{\partial \tau_{t_1}}{\partial t_2}\right)\boldsymbol{n}$. According to Eqs. (9) and (15), and considering the wall shear stress in terms of the surface vorticity components $\boldsymbol{\tau} = (\mu\omega_{t_2}, -\mu\omega_{t_1}, 0)$, Eq. (A1) can be expressed also as:

$$\nabla \times \boldsymbol{\tau} = \left(-\mu\frac{\partial \omega_{t_1}}{\partial t_1} - \mu\frac{\partial \omega_{t_2}}{\partial t_2}\right)\boldsymbol{n} = -\mu\left(\frac{\partial \omega_{t_1}}{\partial t_1} + \frac{\partial \omega_{t_2}}{\partial t_2}\right)\boldsymbol{n}. \quad \text{(A2)}$$

By dividing Eq. (A2) by the density ρ and by considering the dot product between Eq. (A2) and the normal $\boldsymbol{n}$ to the surface $\partial\Omega$, we obtain:

$$\frac{\boldsymbol{n}}{\rho} \cdot (\nabla \times \boldsymbol{\tau}) = -\nu\left(\frac{\partial \omega_{t_1}}{\partial t_1} + \frac{\partial \omega_{t_2}}{\partial t_2}\right) = \sigma_n, \quad \text{(A3)}$$

in accordance with the definition of the vorticity diffusion flux normal to the wall provided in Eq. (12).

REFERENCES

[1]U. Morbiducci, A. M. Kok, B. R. Kwak, P. H. Stone, D. A. Steinman, and J. J. Wentzel, "Atherosclerosis at arterial bifurcations: Evidence for the role of haemodynamics and geometry," Thromb. Haemost. **115**(3), 484–492 (2016).
[2]C. K. Zarins, D. P. Giddens, B. K. Bharadvaj, V. S. Sottiurai, R. F. Mabon, and S. Glagov, "Carotid bifurcation atherosclerosis. Quantitative correlation of

plaque localization with flow velocity profiles and wall shear stress," Circ. Res. **53**(4), 502–514 (1983).
[3]D. N. Ku, D. P. Giddens, C. K. Zarins, and S. Glagov, "Pulsatile flow and atherosclerosis in the human carotid bifurcation. Positive correlation between plaque location and low oscillating shear stress," Arteriosclerosis **5**(3), 293–302 (1985).
[4]C. G. Caro, J. M. Fitz-Gerald, and R. C. Schroter, "Atheroma and arterial wall shear–Observation, correlation and proposal of a shear dependent mass transfer mechanism for atherogenesis," Proc. R. Soc. London. B **177**, 109–133 (1971).
[5]B. R. Kwak, M. Bäck, M.-L. Bochaton-Piallat, G. Caligiuri, M. J. A. P. Daemen, P. F. Davies, I. E. Hoefer, P. Holvoet, H. Jo, R. Krams, S. Lehoux, C. Monaco, S. Steffens, R. Virmani, C. Weber, J. J. Wentzel, and P. C. Evans, "Biomechanical factors in atherosclerosis: Mechanisms and clinical implications," Eur. Heart J. **35**(43), 3013–3020 (2014).
[6]A. Candreva, M. Pagnoni, M. L. Rizzini, T. Mizukami, E. Gallinoro, V. Mazzi, D. Gallo, D. Meier, T. Shinke, J.-P. Aben, S. Nagumo, J. Sonck, D. Munhoz, S. Fournier, E. Barbato, W. Heggermont, S. Cook, C. Chiastra, U. Morbiducci, B. De Bruyne, O. Muller, and C. Collet, "Risk of myocardial infarction based on endothelial shear stress analysis using coronary angiography," Atherosclerosis **342**, 28–35 (2022).
[7]F. J. H. Gijsen, J. J. Wentzel, A. Thury, F. Mastik, J. A. Schaar, J. C. H. Schuurbiers, C. J. Slager, W. J. Van der Giessen, P. J. De Feyter, A. F. W. Van der Steen, and P. W. Serruys, "Strain distribution over plaques in human coronary arteries relates to shear stress," Am. J. Physiol. Heart Circ. Physiol **295**(4), H1608–14 (2008).
[8]G. De Nisco, E. M. J. Hartman, E. Torta, J. Daemen, C. Chiastra, D. Gallo, U. Morbiducci, and J. J. Wentzel, "Predicting lipid-rich plaque progression in coronary arteries using multimodal imaging and wall shear stress signatures," Arterioscler. Thromb. Vasc. Biol. **44**(4), 976–986 (2024).
[9]A. Arzani, A. M. Gambaruto, G. Chen, and S. C. Shadden, "Wall shear stress exposure time: A Lagrangian measure of near-wall stagnation and concentration in cardiovascular flows," Biomech. Model. Mechanobiol. **16**(3), 787–803 (2017).
[10]N. Baeyens, C. Bandyopadhyay, B. G. Coon, S. Yun, and M. A. Schwartz, "Endothelial fluid shear stress sensing in vascular health and disease," J. Clin. Invest **126**(3), 821–828 (2016).
[11]V. Peiffer, S. J. Sherwin, and P. D. Weinberg, "Does low and oscillatory wall shear stress correlate spatially with early atherosclerosis? A systematic review," Cardiovasc. Res. **99**(2), 242–250 (2013).
[12]D. Gallo, P. B. Bijari, U. Morbiducci, Y. Qiao, Y. J. Xie, M. Etesami, D. Habets, E. G. Lakatta, B. A. Wasserman, and D. A. Steinman, "Segment-specific associations between local haemodynamic and imaging markers of early atherosclerosis at the carotid artery: An in vivo human study," J. R Soc. Interface **15**(147), 20180352 (2018).
[13]A. M. Kok, D. S. Molony, L. H. Timmins, Y.-A. Ko, E. Boersma, P. Eshtehardi, J. J. Wentzel, and H. Samady, "The influence of multidirectional shear stress on plaque progression and composition changes in human coronary arteries," EuroIntervention **15**(8), 692–699 (2019).
[14]A. Arzani and S. C. Shadden, "Wall shear stress fixed points in cardiovascular fluid mechanics," J. Biomech. **73**, 145–152 (2018).
[15]V. Mazzi, D. Gallo, K. Calò, M. Najafi, M. O. Khan, G. De Nisco, D. A. Steinman, and U. Morbiducci, "A Eulerian method to analyze wall shear stress fixed points and manifolds in cardiovascular flows," Biomech. Model. Mechanobiol. **19**(5), 1403–1423 (2020).
[16]V. Mazzi, U. Morbiducci, K. Calò, G. De Nisco, M. Lodi Rizzini, E. Torta, G. C. A. Caridi, C. Chiastra, and D. Gallo, "Wall shear stress topological skeleton analysis in cardiovascular flows: Methods and applications," Mathematics **9**(7), 720 (2021).
[17]V. Goodarzi Ardakani, X. Tu, A. M. Gambaruto, I. Velho, J. Tiago, A. Sequeira, and R. Pereira, "Near-wall flow in cerebral aneurysms," Fluids **4**(2), 89 (2019).
[18]H. J. Carpenter, M. H. Ghayesh, A. C. Zander, and P. J. Psaltis, "Effect of coronary artery dynamics on the wall shear stress vector field topological skeleton in fluid–structure interaction analyses," Int. J. Mech. Sys. Dyn. **3**(1), 48–57 (2023).
[19]P. G. Ledda, T. Rossi, M. G. Badas, and G. Querzoli, "Can wall shear-stress topology predict proliferative vitreoretinopathy localization following pars plana vitrectomy?," J. Biomech. **162**, 111914 (2024).
[20]E. Tsolaki, P. Corso, R. Zboray, J. Avaro, C. Appel, M. Liebi, S. Bertazzo, P. P. Heinisch, T. Carrel, D. Obrist, and I. K. Herrmann, "Multiscale multimodal characterization and simulation of structural alterations in failed bioprosthetic heart valves," Acta Biomater. **169**, 138–154 (2023).
[21]U. Morbiducci, V. Mazzi, M. Domanin, G. De Nisco, C. Vergara, D. A. Steinman, and D. Gallo, "Wall shear stress topological skeleton independently predicts long-term restenosis after carotid bifurcation endarterectomy," Ann. Biomed. Eng. **48**(12), 2936–2949 (2020).
[22]V. Mazzi, G. De Nisco, A. Hoogendoorn, K. Calò, C. Chiastra, D. Gallo, D. A. Steinman, J. J. Wentzel, and U. Morbiducci, "Early atherosclerotic changes in coronary arteries are associated with endothelium shear stress contraction/expansion variability," Ann. Biomed. Eng. **49**, 2606 (2021).
[23]M. Mahmoudi, A. Farghadan, D. R. McConnell, A. J. Barker, J. J. Wentzel, M. J. Budoff, and A. Arzani, "The story of wall shear stress in coronary artery atherosclerosis: biochemical transport and mechanotransduction," J. Biomech. Eng **143**(4), 041002 (2021).
[24]V. Mazzi, G. De Nisco, K. Calò, C. Chiastra, J. Daemen, D. A. Steinman, J. J. Wentzel, U. Morbiducci, and D. Gallo, "Divergence of the normalized wall shear stress as an effective computational template of low-density lipoprotein polarization at the arterial blood-vessel wall interface," Comput. Methods Programs Biomed. **226**, 107174 (2022).
[25]D. Küchemann, "Report on the I.U.T.A.M. symposium on concentrated vortex motions in fluids," J. Fluid Mech. **21**(1), 1–20 (1965).
[26]G. Pedrizzetti, G. La Canna, O. Alfieri, and G. Tonti, "The vortex—an early predictor of cardiovascular outcome?," Nat. Rev. Cardiol. **11**(9), 545–553 (2014).
[27]M. Gharib, E. Rambod, A. Kheradvar, D. J. Sahn, and J. O. Dabiri, "Optimal vortex formation as an index of cardiac health," Proc. Natl. Acad. Sci. U. S. A. **103**(16), 6305–6308 (2006).
[28]P. Dyverfeldt, C. Trenti, M. Ziegler, N. Bjarnegård, and M. Lindenberger, "Helical flow in tortuous aortas and its relationship to turbulence: A whole-aorta 4D flow MRI study," Front. Cardiovasc. Med. **10**, 1124604 (2023).
[29]U. Morbiducci, R. Ponzini, G. Rizzo, M. Cadioli, A. Esposito, F. De Cobelli, A. Del Maschio, F. M. Montevecchi, and A. Redaelli, "In vivo quantification of helical blood flow in human aorta by time-resolved three-dimensional cine phase contrast magnetic resonance imaging," Ann. Biomed. Eng. **37**(3), 516–531 (2009).
[30]N. C. Wild, K. V. Bulusu, and M. W. Plesniak, "Vortical structures promote atheroprotective wall shear stress distributions in a carotid artery bifurcation model," Bioengineering **10**(9), 1036 (2023).
[31]D. Gallo, D. A. Steinman, P. B. Bijari, and U. Morbiducci, "Helical flow in carotid bifurcation as surrogate marker of exposure to disturbed shear," J. Biomech. **45**(14), 2398–2404 (2012).
[32]G. De Nisco, A. M. Kok, C. Chiastra, D. Gallo, A. Hoogendoorn, F. Migliavacca, J. J. Wentzel, and U. Morbiducci, "The atheroprotective nature of helical flow in coronary arteries," Ann. Biomed. Eng. **47**(2), 425–438 (2019).
[33]A. Kheradvar and G. Pedrizzetti, *Vortex Formation in the Cardiovascular System* (Springer London, 2012).
[34]N. Tomizawa, S. Fujimoto, T. Mita, D. Takahashi, Y. Nozaki, R. Fan, A. Kudo, Y. Kawaguchi, K. Takamura, M. Hiki, M. Kurita, K. K. Kumamaru, H. Watada, T. Minamino, and S. Aoki, "Coronary artery vorticity to predict functional plaque progression in participants with type 2 diabetes mellitus," Radiol. Cardiothorac. Imaging **5**(4), e230016 (2023).
[35]M. Chu, C. Von Birgelen, Y. Li, J. Westra, J. Yang, N. R. Holm, J. H. C. Reiber, W. Wijns, and S. Tu, "Quantification of disturbed coronary flow by disturbed vorticity index and relation with fractional flow reserve," Atherosclerosis **273**, 136–144 (2018).
[36]M. Lodi Rizzini, A. Candreva, V. Mazzi, M. Pagnoni, C. Chiastra, J.-P. Aben, S. Fournier, S. Cook, O. Muller, B. De Bruyne, T. Mizukami, C. Collet, D. Gallo, and U. Morbiducci, "Blood flow energy identifies coronary lesions culprit of future myocardial infarction," Ann. Biomed. Eng. **52**(2), 226–238 (2024).
[37]N. Varble, G. Trylesinski, J. Xiang, K. Snyder, and H. Meng, "Identification of vortex structures in a cohort of 204 intracranial aneurysms," J. R Soc. Interface **14**(130), 20170021 (2017).
[38]B. J. Chung, F. Mut, C. M. Putman, F. Hamzei-Sichani, W. Brinjikji, D. Kallmes, C. M. Jimenez, and J. R. Cebral, "Identification of hostile

hemodynamics and geometries of cerebral aneurysms: A case-control study," AJNR. Am. J. Neuroradiol. **39**(10), 1860–1866 (2018).
[39]E. L. Leemans, B. M. W. Cornelissen, C. H. Slump, C. B. L. M. Majoie, J. R. Cebral, and H. A. Marquering, "Comparing morphology and hemodynamics of stable-versus-growing and grown intracranial aneurysms," AJNR. Am. J. Neuroradiol. **40**(12), 2102–2110 (2019).
[40]M. Dabagh, P. Nair, J. Gounley, D. Frakes, L. F. Gonzalez, and A. Randles, "Hemodynamic and morphological characteristics of a growing cerebral aneurysm," Neurosurg. Focus **47**(1), E13 (2019).
[41]T. Ngwenya, D. Grundlingh, and M. N. Ngoepe, "Influence of vortical structures on fibrin clot formation in cerebral aneurysms: A two-dimensional computational study," J. Biomech. **165**, 111994 (2024).
[42]J. Biasetti, F. Hussain, and T. C. Gasser, "Blood flow and coherent vortices in the normal and aneurysmatic aortas: A fluid dynamical approach to intraluminal thrombus formation," J. R Soc. Interface **8**(63), 1449–1461 (2011).
[43]A. Arzani and S. C. Shadden, "Characterization of the transport topology in patient-specific abdominal aortic aneurysm models," Phys. Fluids **24**(8), 81901 (2012).
[44]Y. Qiu, J. Wang, J. Zhao, T. Wang, T. Zheng, and D. Yuan, "Association between blood flow pattern and rupture risk of abdominal aortic aneurysm based on computational fluid dynamics," Eur. J. Vasc. Endovasc. Surg. **64**(2–3), 155–164 (2022).
[45]V. Mazzi, D. Gallo, K. Calò, D. A. Steinman, and U. Morbiducci, "Linking wall shear stress and vorticity topologies: Toward a unified theory of cardiovascular flow disturbances," Phys. Fluids **36**(6), 61905 (2024).
[46]M. S. Chong, J. P. Monty, C. Chin, and I. Marusic, "The topology of skin friction and surface vorticity fields in wall-bounded flows," J. Turbul. **13**(null), N6 (2012).
[47]R. C. Chin, J. P. Monty, M. S. Chong, and I. Marusic, "Conditionally averaged flow topology about a critical point pair in the skin friction field of pipe flows using direct numerical simulations," Phys. Rev. Fluids **3**(11), 114607 (2018).
[48]J. Z. Wu and J. M. Wu, "Vorticity dynamics on boundaries," Adv. Appl. Mech. **32**, 119–275 (1996).
[49]A. M. Gambaruto, D. J. Doorly, and T. Yamaguchi, "Wall shear stress and near-wall convective transport: Comparisons with vascular remodelling in a peripheral graft anastomosis," J. Comput. Phys. **229**(14), 5339–5356 (2010).
[50]J. Z. Wu, H. Y. Ma, and M. D. Zhou, *Vorticity and Vortex Dynamics* (Springer Berlin, Heidelberg, 2006).
[51]S. J. Terrington, K. Hourigan, and M. C. Thompson, "The generation and diffusion of vorticity in three-dimensional flows: Lyman's flux," J. Fluid Mech. **915**, A106 (2021).
[52]C. H. Edwards, D. E. Penney, and D. T. Calvis, *Differential Equations and Boundary Value Problems*, 5th ed. (Pearson, 2015).
[53]C. Garth, X. Tricoche, and G. Scheuermann, "Tracking of vector field singularities in unstructured 3D time-dependent datasets," in *Proceedings of IEEE Visualization* (IEEE, 2004), pp. 329–336.
[54]A. M. Gambaruto and A. J. João, "Flow structures in cerebral aneurysms," Comput. Fluids **65**, 56–65 (2012).
[55]C. Chnafa, P. Bouillot, O. Brina, M. Najafi, B. M. A. Delattre, M. I. Vargas, V. M. Pereira, and D. A. Steinman, "Errors in power-law estimations of inflow rates for intracranial aneurysm CFD," J. Biomech. **80**, 159–165 (2018).
[56]N. M. Cancelliere, M. Najafi, O. Brina, P. Bouillot, M. I. Vargas, K.-O. Lovblad, T. Krings, V. M. Pereira, and D. A. Steinman, "4D-CT angiography versus 3D-rotational angiography as the imaging modality for computational fluid dynamics of cerebral aneurysms," J. NeuroIntervent. Surg. **12**(6), 626–LP630 (2020).
[57]C. Liu, Y. Gao, S. Tian, and X. Dong, "Rortex – A new vortex vector definition and vorticity tensor and vector decompositions," Phys. Fluids **30**(3), 035103 (2018).
[58]S. Tian, Y. Gao, X. Dong, and C. Liu, "Definitions of vortex vector and vortex," J. Fluid Mech. **849**, 312–339 (2018).
[59]Y. Wang, Y. Gao, J. Liu, and C. Liu, "Explicit formula for the Liutex vector and physical meaning of vorticity based on the Liutex-Shear decomposition," J. Hydrodyn. **31**(3), 464–474 (2019).
[60]B. Pang, Y. Ding, and Y. Wang, "Flow behavior analysis in boundary layer transition based on the Liutex–shear decomposition," AIP Adv **13**(2), 025244 (2023).
[61]P. Shrestha, C. Nottage, Y. Yu, O. Alvarez, and C. Liu, "Stretching and shearing contamination analysis for Liutex and other vortex identification methods," Adv. Aerodyn. **3**(1), 8 (2021).
[62]A. Arzani, A. M. Gambaruto, G. Chen, and S. C. Shadden, "Lagrangian wall shear stress structures and near-wall transport in high-Schmidt-number aneurysmal flows," J. Fluid Mech. **790**, 158–172 (2016).
[63]D. A. Steinman and V. M. Pereira, "How patient specific are patient-specific computational models of cerebral aneurysms? An overview of sources of error and variability," Neurosurg. Focus. **47**(1), E14 (2019).
[64]A. E. Perry and B. D. Fairlie, in *International Union of Theoretical and Applied Mechanics; International Union of Geodesy and Geophysics* (Elsevier, 1975), pp. 299–315.